



## Ultrasonic guided wave scattering due to delamination in curved composite structures

Rajendra Kumar Munian, D. Roy Mahapatra\*, S. Gopalakrishnan

*Department of Aerospace Engineering, Indian Institute of Science, Bangalore 560012, India*

### ARTICLE INFO

**Keywords:**

Delamination  
Guided wave  
Curved structure  
Joint  
Spectral finite element method  
Damage detection

### ABSTRACT

Wave propagation in a curved composite structure having delamination is simulated using time domain spectral finite element (TSFE) method that enables fast computation with higher-order field interpolation. Curved structures are very common in aerospace, marine and other composite structural components and understanding ways to detect delamination in these curved structures with the help of ultrasonic guided wave simulation is essential. Guided wave interaction with curved region progressively causes mode converted waves, which are present in both reflected as well as transmitted wave packets. The details are poorly understood. The additional wave packets due to interaction cause difficulty in identification of damaged induced responses. Mode conversion and reflection from the curved section reduce the useful signal strength to interrogate any delamination in the curved region. Guided wave interaction with the curved section in an L-shaped structure and a structure with T-joint are studied using TSFE simulation. Simulation results are validated using analytical solutions. Mode conversion and transmission in T-joint is studied using numerical simulation with experimental validation. Signal loss due to mode conversion and reflections at different frequencies is investigated in terms of geometric and wave parameters, which promises to identify the appropriate frequencies and choice of wave mode for monitoring.

### 1. Introduction

Ultrasonic guided wave-based damage detection schemes have certain advantages over other non-destructive inspection techniques because of its ability to cover a larger area of inspection in thin to moderately thick composite structures, where specific physics of individual wave modes can be designed to amplify specific type of damages. The schemes allow a network of transducers to be integrated into a composite structure for both offline periodic inspection as well as online monitoring with minimal preparation on ground as compared to current inspection practices for aerospace/marine composite structures [1–3]. Guided wave propagation in flat plates have been extensively studied [1]. Similar wave modes in cylindrical metallic pipes have also been studied extensively [4,5]. However, the nature of wave mode conversion and scattering due to defects in the composite pipes are less explored [6,7] and also those aspects are poorly understood in case of progressively varying curvature of a curved section of a composite laminate. Curved composite structures are quite common in aircraft and marine vehicle structures [8,9]. They are generally thin-walled, typically designed with respect to compressive strength due to delamination after impact [10]. Ultrasonic guided waves are well suited for

inspection of delamination in composite structures in general due to the fact that defects are hidden inside the structure and ultrasonic or X-ray scan or tomography can provide such hidden features although such scan requires elaborate preparation and not suitable to large-scale structural inspection. A curvature in the waveguide causes reflection as well as mode converted waves [11] and such behavior is dependent on the wavelength. The strength of the mode converted waves is dependent on whether the curvature is sudden or gradual. A single wave mode is desired in the inspection of delamination as it makes correlation to defect parameters simple. Presence of multiple wave modes in the signal makes the identification of defect features more difficult. However, mode conversion at the curved region can produce other wave modes in both the reflected and transmitted waves. When the waves propagate through a curved segment, the signal energy may decay differently as compared to that in plane waves having cylindrical loss. Therefore, a detailed understanding of guided wave mode interaction in the curved region is required so that an appropriate choice of frequency and wave modes can be used to inspect a delamination of certain probable size in the curved region. Eventually, such details will be useful in signal processing toward reliable prediction of delamination in curved composite structures using ultrasonic guided waves.

\* Corresponding author.

E-mail address: [roymahapatra@iisc.ac.in](mailto:roymahapatra@iisc.ac.in) (D. Roy Mahapatra).

Nomenclature	
$u, v$	Displacement fields in $x$ and $y$ direction
$P_m$	Legendre polynomial of order $m$
$u_k, v_k$	Nodal displacement of $k^{\text{th}}$ node in an element
$\phi_k$	Shape function corresponding to node $k$
$M, K, f$	Mass, stiffness matrices and force vector
$B$	Strain displacement transformation matrix
$N$	Shape function matrix
$\delta_{ij}$	Kronecker delta
$x', y'$	Local coordinate system in curved beam
$u', v'$	Displacement fields with respect to local coordinate system $(x', y')$
$f_y, f_x, M'$	Local cross-sectional force in $x'$ and $y'$ direction, and moment at a point
$A_{11}, A_{33}, D_{11}$	Cross-sectional stiffness coefficients
$J_0, J_2$	0 <sup>th</sup> and 2 <sup>nd</sup> mass moment of a cross section
$r, \theta$	Radial distance and angular coordinate in radial coordinate system
$R$	Radius of curvature of mid-plane in curved beam
$u_0, v_0$	Displacement of mid-plane in local coordinate system $(x', y')$
$E_{11}, G_{12}$	Modulus of elasticity in longitudinal direction of fiber and shear modulus
$k_i^{(p)}$	$i^{\text{th}}$ wavenumber corresponding to medium- $p$
$\hat{\mathbf{u}}_1^{(p)}$	Incident displacements at port-1 in frequency domain
$\bar{\mathbf{u}}_j^{(p)}$	Eigenvector corresponding to $j^{\text{th}}$ wavenumber ( $k_j^{(p)}$ ) in medium- $p$
$\bar{\mathbf{U}}_f^{(p)}, \bar{\mathbf{U}}_b^{(p)}$	Eigenvector matrix corresponding to wavenumbers of forward and backward propagating waves in medium- $p$
$\hat{\mathbf{u}}_f^{(p)}, \hat{\mathbf{u}}_b^{(p)}$	Frequency domain displacement fields (vector) due to forward and backward propagating waves in medium- $p$
$\mathbf{c}_f^{(p)}, \mathbf{c}_b^{(p)}$	Coefficients for forward and backward propagating waves in medium- $p$
$\hat{P}_{11}, \hat{P}_{01}$	Frequency domain power inflow and power outflow through port-1
$\hat{P}_{11(S_0)}, \hat{P}_{11(A_0)}$	Frequency domain power inflow through port-1 due to inflowing $S_0$ and $A_0$ waves, respectively
$\hat{P}_{01(S_0)}, \hat{P}_{01(A_0)}$	Frequency domain power outflow due to reflected $S_0$ and $A_0$ waves, respectively at port-1
$\hat{P}_{02(S_0)}, \hat{P}_{02(A_0)}$	Frequency domain power outflow due to reflected $S_0$ and $A_0$ waves, respectively at port-2
$S_{ij(S_0-A_0)}$	Scattering coefficient in terms of power flow corresponding to $A_0$ wave outflow through port- $i$ caused by $S_0$ wave inflow through port- $j$
$\bar{S}_{ij(A_0-S_0)}$	Scattering coefficients in terms of signal energy corresponding to $S_0$ wave outflow at port- $i$ due to $A_0$ wave inflow at port- $j$

There are some experimental studies which reported longitudinal, flexural [12,13] and torsional wave [14] interaction with damage in curved pipes with elbow joints. Experiments were performed for inspection of stiffened panels [15–17] using guided waves. Mahapatra and Gopalakrishnan [18] studied the guided wave scattering from angled joint formed due to multiply connected composite beams and studied the effect of angle on mode conversion. Recent work on defect detection in curved composite winglet using guided waves has been reported [19]. Ramadas et al. [20] observed mode conversion and turning wave modes due to fundamental antisymmetric ( $A_0$ ) wave interaction with shell skin and spar joint.

Composite structural joints are one of the important structural elements for transferring the load from one component to another. Unlike metallic structures, rivet joints are not a feasible and effective option to assemble structural components made of composites. Co-bonded and sometimes co-cured integrated joints are commonly used. This kind of assembly can reduce the use of fasteners and drilled holes, which makes the structure optimized in terms of both weight reduction and stress concentrators. Under various loading conditions, especially tensile [21] or bending [22] loading, the interlaminar crack may form in the junction. There are various methods available to detect defects in such kind of structures, however, most of those are local methods. Therefore, inspection using this method has to be carried out offline. The guided wave-based detection technique is better suited to inspect such geometrically complicated structures [23,24,25] online. Geetha et al. [23] investigated ultrasonic guided wave interaction with delamination in composite T-joint in web-flange interface using laser Doppler imaging technique and observed wave mode conversion. Effect of delamination edges with respect to the incident waves at the T-joint was studied in detail. However, the effect of curvature on such detection process is not reported till date and this particular aspect will be discussed in the present paper. Recently Philibert et al. [26] used guided waves to detect impact damages including matrix crack and delamination in composite T-joint using guided waves. However, defect detection methodologies using guided waves in such complex structures are yet to be developed. A lot of research based on the theoretical understanding and simulation are required for establishing inspection and monitoring method for curved structures with damage tolerant characteristics.

Theoretical development of elastic wave propagation in the curved

structures was started by Morley [27]. Morley developed Timoshenko-type theory to study flexural wave propagation in a slightly curved infinite rod. Later, wave propagation in isotropic curved beams, ring arches and helical structures [28–32] were studied. Crowley et al. [28] used the Morley's theory and studied wave propagation in a rectangular beam showing wavefield from the numerical solutions backed by experimental study. Graff [30] derived equations for vibrational power transmission in a ring and accounted for extensional, shear and rotary inertia effects in wave dispersion relation. Curvature effect produces the coupled wave modes (both axial and flexural waves) in a beam and it depends on the radius of curvature of the medium [29]. This effect is somewhat similar to wave mode conversion due to asymmetric ply stacking as studied considering sharp curvature or multiple member joint [18] and also due to ply drop or asymmetrically located delamination [33]. Treyssede [32] studied three-dimensional curvature effect on wave propagation in helical structure for different cross-section radius and lay angle, and investigated mode conversions and scattering due to inhomogeneity. Coupled wave propagation in a composite tubular structure where translational, rotational and warping motions are considered, are modeled and effects of fiber orientation in wave responses are studied [34]. Nanda and Kapuria [35] studied the wave propagation in a curved composite beam using both classical laminate theory and first-order shear deformation theory (FSDT) at low as well as the high frequencies for beams with different curvature and thickness using frequency domain spectral element method. Their work showed that there is a significant difference between the responses predicted by classical laminate theory and first-order shear deformation theory when curvature effect is present. Wave mode conversion, reflection, and transmission due to change in sectional curvature are estimated and presented using an analytical method for isotropic [36,37] and composites beams [38]. Wave propagation in a curved structure has been studied in the context of vibration and noise control. Bot et al. [39] studied the energy flow in Love–Kirchhoff curved beam for longitudinal as well as flexural waves using energy density model. Lee et al. [40] studied wave propagation through the U-shaped beam and analyzed the reflection and transmission through the U-region. Jeong and Ih [41] studied the wave propagation in curved structure and investigated the power flow through the curved region using a ray tracing method. Curvature effect in a plate on wave propagation is studied by Fong and

Lowe [42] using an analytical approach, which is validated by the experimental result, and they predicted various lower order modes in plates. Theoretical development of circumferential waves in a curved isotropic and layered plate is found in literature [43]. Effect of defect considering these background effects were not studied.

All the above studies used simplified models for curved structures without the localized effect of defects being accurately modeled where the regime of length-scale in terms of radius of curvature, thickness and wavelength strongly influence the behavior which needs to be understood clearly. In order to deal with multilayered composite curved structure, finite element method is an important tool to model without losing much generality. Zhou and Ichchou [44] studied the wave propagation in curved pipes using wave based finite element method which is a method that extracts the eigenmodes using finite element method, and wave propagation characteristics in the structure are represented using those eigenmodes. Reflection and transmission at different frequencies are also studied by the same authors. Demma et al. [11] studied the reflection and transmission of the longitudinal and torsional waves in pipes using finite element analysis, dispersion curve for curved pipe was computed using FE analysis [45]. Aristegui et al. [46] studied the wave propagation in curved pipes and determined the wave mode conversion and transmissibility using finite element method. Sanderson et al. [47] developed analytical methodologies for wave transmission through curved pipes using information obtained finite element simulation results. Wide number of literature reports finite element method as a powerful numerical tool to model wave propagation in a complex structure with defects. Wave propagation and scattering based detection of defects require adequately high-frequency excitation to localize the waves with high phase contrast around the defect boundaries. Modeling such kind of high-frequency waves by finite element method requires very fine mesh and thereby makes large area simulation computationally prohibitive. Time domain spectral finite element (TSFE) is advantageous for such kind of problem [48]. The method relies on field interpolation with higher-order function having spectral convergence properties and it has been widely used in various fields of science and engineering for its numerical efficiency. TSFE was first introduced by Patera [49]. Later, the potential of TSFE was recognized and applied in various fields of science and engineering. TSFE method was applied to fluid mechanics problems [50], elastic wave propagation in structure [51], seismic vibration [52], and acoustic [53] analysis.

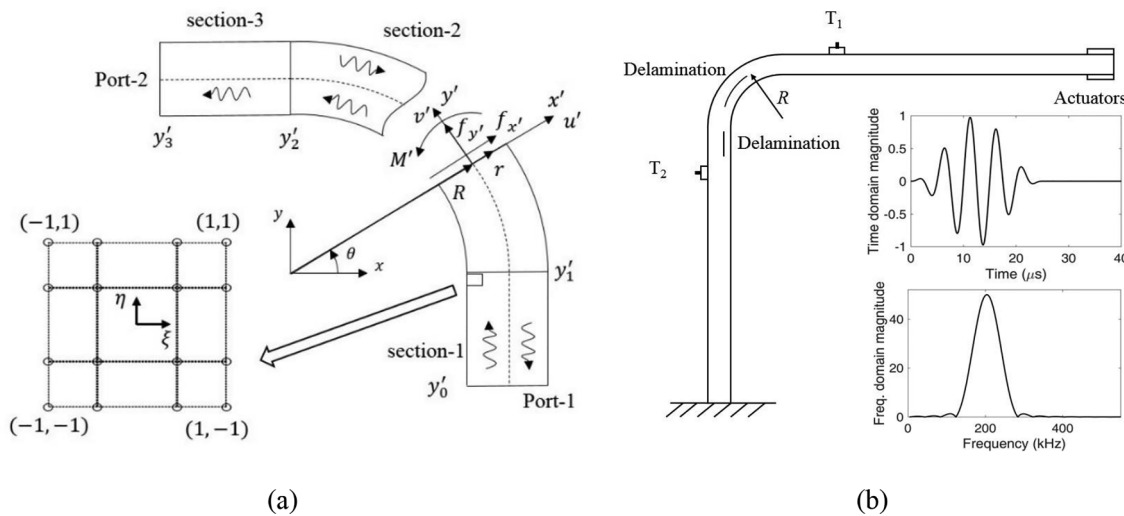


**Fig. 1.** (a) Schematic of a curved beam segment, and wave scattering from L-segment, along with port definition used in the simulation; representative 16-noded spectral element (shown in inset) (b) Laminated composite component with curvature, a pair of actuator mounted at the free edge of the horizontal section, the sensor at T<sub>1</sub> for capturing incident and reflected waves and the sensor at T<sub>2</sub> for capturing transmitted waves, Hanning windowed sinusoidal excitation signal and frequency spectra of excitation signal (shown in inset).

## 2. Mathematical formulation

### 2.1. TSFE formulation

A two-dimensional domain  $\Omega$  with uniform thickness  $h$  under in-plane loading is considered. Within the domain, strains due to the in-plane displacements  $u(x, y)$  and  $v(x, y)$  contribute to the total strain energy. For finite element formulation, the entire domain is divided into a finite number of elements (sub-domains). Geometry is defined using global coordinates  $(x, y)$ . For elemental formulation, a local coordinate system  $(\xi, \eta)$  is defined. In reference element, nodes are based on Lobatto point distributions, where, in a particular coordinate direction, nodes are chosen as roots of the following equations

$$(1 - \xi^2) \frac{dP_m(\xi)}{d\xi} = 0, (1 - \eta^2) \frac{dP_m(\eta)}{d\eta} = 0 \quad (1)$$

where  $P_m(\xi)$  is the Legendre polynomial and subscript denotes the order of the polynomial. In the reference element, both the coordinates  $\xi$  and  $\eta$  vary in the range  $[-1, 1]$ . Displacement fields are approximated using  $m^{\text{th}}$  order interpolation polynomial in both the direction, hence, there are total  $s = (m + 1) \times (m + 1)$  number of nodes distributed in an element. TSFE is very similar to the traditional finite element method, the major difference is that the TSFE uses nodes based on the Chebyshev or Lobatto nodal distribution, which place nodes denser near the edges. Nodal distribution based on Lobatto points of a 16 node element is shown in Fig. 1(a) for example. For the given nodal distributions in reference element, a set of shape functions are constructed. Displacement fields are approximated using those shape function as

$$u(\xi, \eta, t) = \sum_{k=1}^s \phi_k(\xi, \eta) u_k(t) \quad (2)$$

$$v(\xi, \eta, t) = \sum_{k=1}^s \phi_k(\xi, \eta) v_k(t) \quad (3)$$

where  $u_k(t)$  and  $v_k(t)$  denote the nodal displacements corresponding to  $k^{\text{th}}$  node in the element.  $u(\xi, \eta, t)$  and  $v(\xi, \eta, t)$  are the displacement fields in the element in the direction of  $x$  and  $y$  directions respectively.  $\phi_k(\xi, \eta)$  is the two-dimensional shape function in the reference element corresponding to  $k^{\text{th}}$  node. Considering,  $k^{\text{th}}$  node in reference element is located  $i^{\text{th}}$  and  $j^{\text{th}}$  position in  $\xi$  and  $\eta$  direction, respectively, the shape function  $\phi_k(\xi, \eta)$  is expressed as

$$\phi_k(\xi, \eta) = \left[ \prod_{p=1, p \neq i}^{m+1} \frac{(\xi - \xi_p)}{(\xi_i - \xi_p)} \right] \left[ \prod_{q=1, q \neq j}^{m+1} \frac{(\eta - \eta_q)}{(\eta_j - \eta_q)} \right] \quad (4)$$

Displacement fields are written in terms of the nodal displacements using shape function matrix as

$$\begin{cases} u(\xi, \eta, t) \\ v(\xi, \eta, t) \end{cases} = \sum_{k=1}^s \begin{bmatrix} \phi_k(\xi, \eta) & 0 \\ 0 & \phi_k(\xi, \eta) \end{bmatrix} \begin{cases} u_k(t) \\ v_k(t) \end{cases} = \sum_{k=1}^s [N_k(\xi, \eta)] \begin{cases} u_k(t) \\ v_k(t) \end{cases} = \mathbf{N}\mathbf{u}(t) \quad (5)$$

where  $\mathbf{N}$  is the shape function matrix which is the function of local spatial coordinates  $\xi$  and  $\eta$ .  $\mathbf{u}(t)$  is the elemental nodal displacement vector dependent on time. Using the displacement field given in Eq. (5), governing system of equations for an element can be obtained using standard finite element formulation [57] and the elemental equation can be written as

$$\mathbf{M}\ddot{\mathbf{u}} + \mathbf{K}\mathbf{u} = \mathbf{f} \quad (6)$$

where the elemental mass ( $\mathbf{M}$ ), stiffness matrices ( $\mathbf{K}$ ) and force vector ( $\mathbf{f}$ ) are calculated as

$$\mathbf{M} = \int_{-1}^1 \int_{-1}^1 \mathbf{N}^T(\xi, \eta) \rho \mathbf{N}(\xi, \eta) |\mathbf{J}(\xi, \eta)| h d\xi d\eta \quad (7)$$

$$\mathbf{K} = \int_{-1}^1 \int_{-1}^1 \mathbf{B}^T(\xi, \eta) \mathbf{E} \mathbf{B}(\xi, \eta) |\mathbf{J}(\xi, \eta)| h d\xi d\eta \quad (8)$$

$$\mathbf{f} = \int_{\Gamma_e} \mathbf{N}^T \mathbf{f} d\Gamma_e \quad (9)$$

where  $\mathbf{B}(\xi, \eta)$  is the strain displacement matrix,  $\mathbf{f}$  is the force field vector acting on the body in the plane of the geometry. Elemental Eq. (6) are calculated and assembled over the entire domain to obtain the global system of equations. In this Legendre polynomial based spectral element formulation, Gauss-Legendre-Lobatto quadrature rule is used for numerical integration. The integration points coincide with the nodal points. Shape functions have the following property

$$\phi_i(\xi_j, \eta_j) = \delta_{ij} \quad (10)$$

In the spectral element formulation, a submatrix of an element mass matrix is expressed as

$$M_{pq} = \sum_k \begin{bmatrix} w_k \rho \phi_i(\xi_k, \eta_k) \phi_j(\xi_k, \eta_k) & 0 \\ 0 & w_k \rho \phi_p(\xi_k, \eta_k) \phi_q(\xi_k, \eta_k) \end{bmatrix} h |\mathbf{J}(\xi_k, \eta_k)| \quad (11)$$

where  $w_k$  are the integration weights corresponding to  $k^{\text{th}}$  integration point. Considering the shape function properties

$$\sum_k \phi_p(\xi_k, \eta_k) \phi_q(\xi_k, \eta_k) = \sum_k \delta_{pk} \delta_{qk} = \delta_{pq} \quad (12)$$

where  $(\xi_k, \eta_k)$  is the nodal coordinate corresponding to node number  $k$  and  $\delta_{pq}$  is the Kronecker delta, and this property results in a diagonal mass matrix. Using this property, we get

$$\sum_k \rho h w_k \phi_p(\xi_k, \eta_k) \phi_q(\xi_k, \eta_k) |\mathbf{J}(\xi_k, \eta_k)| = \rho h w_p \delta_{pq} |\mathbf{J}(\xi_p, \eta_p)| \quad (13)$$

From the above conditions, we get the submatrix  $M_{pq}$  which can be written as

$$M_{pq} = \begin{cases} \begin{bmatrix} H_p & 0 \\ 0 & H_p \end{bmatrix} & \text{when } p = q = k \\ \begin{bmatrix} 0 & 0 \\ 0 & 0 \end{bmatrix} & \text{when } p \neq q, \text{ or } q \neq k, \text{ or } p \neq k \end{cases} \quad (14)$$

where  $H_p$  is a constant. The condition given in Eq. (14) makes the mass matrix diagonal and reduces the memory required for matrix storage. In the process of mass matrix diagonalization, the accuracy of the mass matrix is compromised only by the choice of the number of terms taken in the integration or the number of nodes in the element. However, due to the spectral or higher-order convergence properties of the interpolation field, the spectral method reduces the error in the mass matrix calculation significantly. TSFE uses higher-order interpolation polynomial which can efficiently capture the higher-order displacement fields produced by the wave fields due to high-frequency excitation. Spectral convergence along with reduced memory requirement due to diagonal mass matrix makes TSFE a computationally efficient scheme. With these advantages, TSFE is employed to investigate wave interaction with curved composite laminate with defects.

### 2.2. Scattering coefficient calculation

Wave scattering in the curved region causes reflection, transmission and mode conversions. The scattering coefficients in terms of power flow are calculated analytically using first-order shear deformation theory (FSDT) and compared with the numerical simulation results using TSFE. The undeformed coordinate and small displacement of a point in the curved beam is expressed in the polar coordinate system  $(r, \theta)$ . Consider a local coordinate system  $(x', y')$  and displacements in corresponding coordinate direction are  $u'$  and  $v'$ , respectively, as shown in Fig. 1(a). Coordinate  $x'$  is measured from the midplane of the beam in the direction of  $r$ .  $x'$  is expressed as  $x' = r - R$ .  $y'$  is in the tangential direction of the beam. We neglect the variation of radial displacement across the thickness. Using FSDT approximation, displacement fields in local transverse and axial direction can be expressed as

$$u'(x', y', t) = u'_0(y', t) \quad (15)$$

$$v'(x', y', t) = v'_0(y', t) + x'\theta'(y', t) \quad (16)$$

where  $u'_0$  and  $v'_0$  are the midplane displacement in  $x'$  and  $y'$  direction respectively. And  $\theta'$  is the rotation of the cross-section in anti-clockwise direction. Considering thickness of the beam is very small with respect to radius of curvature ( $R$ ) of mid-plane of the beam, strains in local coordinate system are given as

$$\varepsilon_{x'x'} \approx \frac{\partial u'}{\partial r} \approx \frac{\partial u'}{\partial x'} = 0 \quad (17)$$

$$\varepsilon_{y'y'} \approx \frac{u'}{r} + \frac{1}{r} \frac{\partial v'}{\partial \theta} \quad (18)$$

$$\gamma_{x'y'} \approx \frac{1}{r} \frac{\partial u'}{\partial \theta} + \frac{\partial v'}{\partial r} - \frac{v'}{r} \quad (19)$$

Considering thickness is very small we assume  $r \approx R$ ,  $rd\theta = dy'$ , and Eq. (18) can be written as

$$\varepsilon_{y'y'} = \frac{u'}{R} + \frac{\partial v'}{\partial y'} \quad (20)$$

Similarly, Eq. (19) can be written as

$$\gamma_{x'y'} = \frac{\partial u'}{\partial y'} + \frac{\partial v'}{\partial x'} - \frac{v'}{R} \quad (21)$$

Inserting expressions of  $u'$  and  $v'$  from Eqs. (15) and (16) into the Eqs. (20) and (21) we get the local axial normal strain  $\varepsilon_{y'y'}$ , and the transverse shear strain  $\gamma_{x'y'}$  as

$$\varepsilon_{y'y'} = \frac{u'_0}{R} + \frac{\partial v'_0}{\partial y'} + x' \frac{\partial \theta'}{\partial y'}, \quad \gamma_{x'y'} = \frac{\partial u'_0}{\partial y'} - \frac{v'_0}{R} + \theta' \quad (22)$$

Axial normal stress  $\sigma_{y'y'}$  and shear stress  $\tau_{x'y'}$  are given by

$$\sigma_{y'y'} = E_{11} \left( \frac{u'_0}{R} + \frac{\partial v'_0}{\partial y'} + x' \frac{\partial \theta'}{\partial y'} \right), \quad \tau_{x'y'} = G_{12} \kappa \left( \frac{\partial u'_0}{\partial y'} - \frac{v'_0}{R} + \theta' \right) \quad (23)$$

where  $E_{11}$  is the modulus of elasticity in the longitudinal direction of fiber orientation and  $G_{12}$  is the shear modulus,  $\kappa$  is shear correction factor. The local axial force, shear force and bending moment are expressed as

$$\begin{aligned} f_{y'} &= \int_{-\frac{h}{2}}^{\frac{h}{2}} \sigma_{y'y'} b dx' = \int_{-\frac{h}{2}}^{\frac{h}{2}} E_{11} \left( \frac{u'_0}{R} + \frac{\partial v'_0}{\partial y'} + x' \frac{\partial \theta'}{\partial y'} \right) b dx' \\ &= A_{11} \left( \frac{u'_0}{R} + \frac{\partial v'_0}{\partial y'} \right) \end{aligned} \quad (24)$$

$$\begin{aligned} f_{x'} &= \int_{-\frac{h}{2}}^{\frac{h}{2}} \tau_{x'y'} b dx' = \int_{-\frac{h}{2}}^{\frac{h}{2}} G_{12} \kappa \left( \frac{\partial u'_0}{\partial y'} - \frac{v'_0}{R} + \theta' \right) b dx' \\ &= A_{33} \left( \frac{\partial u'_0}{\partial y'} - \frac{v'_0}{R} + \theta' \right) \end{aligned} \quad (25)$$

$$\begin{aligned} M' &= \int_{-\frac{h}{2}}^{\frac{h}{2}} x' \sigma_{y'y'} b dx' = \int_{-\frac{h}{2}}^{\frac{h}{2}} x' E_{11} \left( \frac{u'_0}{R} + \frac{\partial v'_0}{\partial y'} + x' \frac{\partial \theta'}{\partial y'} \right) b dx' \\ &= D_{11} \left( \frac{u'_0}{R} + \frac{\partial v'_0}{\partial y'} \right) \end{aligned} \quad (26)$$

where  $h$  is the thickness and  $b$  is the width of the beam,  $A_{11}$ ,  $A_{33}$  and  $D_{11}$  are the cross-sectional stiffness coefficients for a laminate, which are expressed as

$$\begin{aligned} A_{11} &= \sum_{j=1}^n (E_{11})_j (x'_j - x'_{j-1}), \quad A_{33} = \sum_{j=1}^n (\kappa G_{12})_j (x'_j - x'_{j-1}), \quad D_{11} \\ &= \frac{1}{3} \sum_{j=1}^n (E_{11})_j (x'^3_j - x'^3_{j-1}), \quad J_0 = \sum_{j=1}^n \rho (x'_j - x'_{j-1}), \quad J_2 \\ &= \frac{1}{3} \sum_{j=1}^n \rho (x'^3_j - x'^3_{j-1}) \end{aligned} \quad (27)$$

We apply Hamilton's principle to obtain the governing differential equations which are of the following forms

$$-\frac{A_{11}}{R} \frac{\partial u'_0}{\partial y'} - A_{11} \frac{\partial^2 v'_0}{\partial y'^2} - \frac{A_{33}}{R} \frac{\partial u'_0}{\partial y'} + \frac{A_{33}}{R^2} v'_0 - \frac{A_{33}}{R} \theta' + I_0 \ddot{v}'_0 = 0 \quad (28)$$

$$\frac{A_{11}}{R^2} u'_0 + \frac{A_{11}}{R} \frac{\partial v'_0}{\partial y'} - A_{33} \frac{\partial^2 u'_0}{\partial y'^2} + \frac{A_{33}}{R} \frac{\partial v'_0}{\partial y'} - A_{33} \frac{\partial \theta'}{\partial y'} + I_0 \ddot{u}'_0 = 0 \quad (29)$$

$$-D_{11} \frac{\partial^2 \theta'}{\partial y'^2} + A_{33} \frac{\partial u'_0}{\partial y'} - \frac{A_{33}}{R} v'_0 + A_{33} \theta' + I_2 \ddot{\theta}' = 0 \quad (30)$$

In order to find the general solutions of the above system of differential equations, we assume solutions in frequency-wavenumber space

$$v'_0(y', t) = \hat{v}'_0 e^{-i(ky' - \omega t)} \quad (31)$$

$$u'_0(y', t) = \hat{u}'_0 e^{-i(ky' - \omega t)} \quad (32)$$

$$\theta'(y', t) = \hat{\theta}' e^{-i(ky' - \omega t)} \quad (33)$$

After applying the relations given in Eqs. (31)–(33) to the governing differential Eqs. (28)–(30), the spectrum relations are obtained as

$$\left( A_{11} k^2 + \frac{A_{33}}{R^2} - I_0 \omega^2 \right) \hat{v}'_0 + \left( i \frac{A_{11}}{R} k + i \frac{A_{33}}{R} k \right) \hat{u}'_0 + \left( -\frac{A_{33}}{R} \right) \hat{\theta}' = 0 \quad (34)$$

$$\left( -i \frac{A_{11}}{R} k - i \frac{A_{33}}{R} k \right) \hat{v}'_0 + \left( A_{33} k^2 + \frac{A_{11}}{R^2} - I_0 \omega^2 \right) \hat{u}'_0 + (i A_{33} k) \hat{\theta}' = 0 \quad (35)$$

$$\left( -\frac{A_{33}}{R} \right) \hat{v}'_0 + (-i A_{33} k) \hat{u}'_0 + (D_{11} k^2 + A_{33} - I_2 \omega^2) \hat{\theta}' = 0 \quad (36)$$

Eqs. (34)–(36) can be written in the form of a polynomial eigenvalue problem, that is,

$$\begin{cases} \begin{bmatrix} A_{11} & 0 & 0 \\ 0 & A_{33} & 0 \\ 0 & 0 & D_{11} \end{bmatrix} k^2 + \begin{bmatrix} 0 & i \frac{A_{11}}{R} + i \frac{A_{33}}{R} & 0 \\ -i \frac{A_{11}}{R} - i \frac{A_{33}}{R} & 0 & i A_{33} \\ 0 & -i A_{33} & 0 \end{bmatrix} k \\ + \begin{bmatrix} \frac{A_{33}}{R^2} - I_0 \omega^2 & 0 & -\frac{A_{33}}{R} \\ 0 & \frac{A_{11}}{R^2} - I_0 \omega^2 & 0 \\ -\frac{A_{33}}{R} & 0 & A_{33} - I_2 \omega^2 \end{bmatrix} \end{cases} \begin{bmatrix} \hat{v}'_0 \\ \hat{u}'_0 \\ \hat{\theta}' \end{bmatrix} = 0 \quad (37)$$

The above polynomial eigenvalue problem has six eigenvalues which are the values for wavenumber ( $k$ ) and the corresponding six eigenvectors at each frequency. In the current problem, the entire domain is considered to be an assembly of multiple sections with different radius of curvature as shown in Fig. 1(a). Therefore, different sections have different dispersion behavior. Let us consider a medium  $p$  having all the quantities denoted as  $(.)^{(p)}$ . In the medium, the wavenumbers are  $k_1^{(p)}, k_2^{(p)}, \dots, k_6^{(p)}$  and the corresponding eigen vectors are  $\bar{u}_1^{(p)}, \bar{u}_2^{(p)}, \dots, \bar{u}_6^{(p)}$ . The eigen vector corresponding to  $j^{\text{th}}$  wavenumber  $k_j^{(p)}$  is written as

$$\bar{u}_j^{(p)} = \{u_{1j}^{(p)}, u_{2j}^{(p)}, u_{3j}^{(p)}\}^T. \quad (38)$$

For each frequency, out of the six wavenumbers and the same number of eigenvectors, three are forward propagating waves and rest

**Table 1**  
Material properties of orthotropic layer in composite laminate.

E <sub>11</sub> (GPa)	E <sub>22</sub> , E <sub>33</sub> (GPa)	G <sub>12</sub> , G <sub>13</sub> (GPa)	G <sub>23</sub> (GPa)	ν <sub>12</sub> , ν <sub>13</sub>	ρ (kg/m <sup>3</sup> )
144.8	9.65	4.14	3.45	0.3	1389

three are the backward propagating waves. Let us consider, wave-numbers  $k_1^{(p)}, k_2^{(p)}, k_3^{(p)}$  and the corresponding eigenvectors  $\bar{\mathbf{u}}_1^{(p)}, \bar{\mathbf{u}}_2^{(p)}, \bar{\mathbf{u}}_3^{(p)}$  represent the forward propagating waves. The wave-numbers  $k_4^{(p)}, k_5^{(p)}, k_6^{(p)}$  and the corresponding eigenvectors  $\bar{\mathbf{u}}_4^{(p)}, \bar{\mathbf{u}}_5^{(p)}, \bar{\mathbf{u}}_6^{(p)}$  represent the backward propagating waves. The generalized displacement field is contributed by the forward and backward propagating waves. Total displacement field in the frequency domain can be expressed in matrix–vector form as

$$\hat{\mathbf{u}}^{(p)} = \left\{ \hat{v}_0^{(p)}, \hat{u}_0^{(p)}, \hat{\theta}'^{(p)} \right\}^T = \hat{\mathbf{u}}_f^{(p)} + \hat{\mathbf{u}}_b^{(p)} = \bar{\mathbf{U}}_f^{(p)} \Lambda_f^{(p)}(y') \mathbf{c}_f^{(p)} + \bar{\mathbf{U}}_b^{(p)} \Lambda_b^{(p)}(y') \mathbf{c}_b^{(p)} \quad (39)$$

where  $(.)_f$  indicates the forward and  $(.)_b$  indicates the backward propagating wave components,

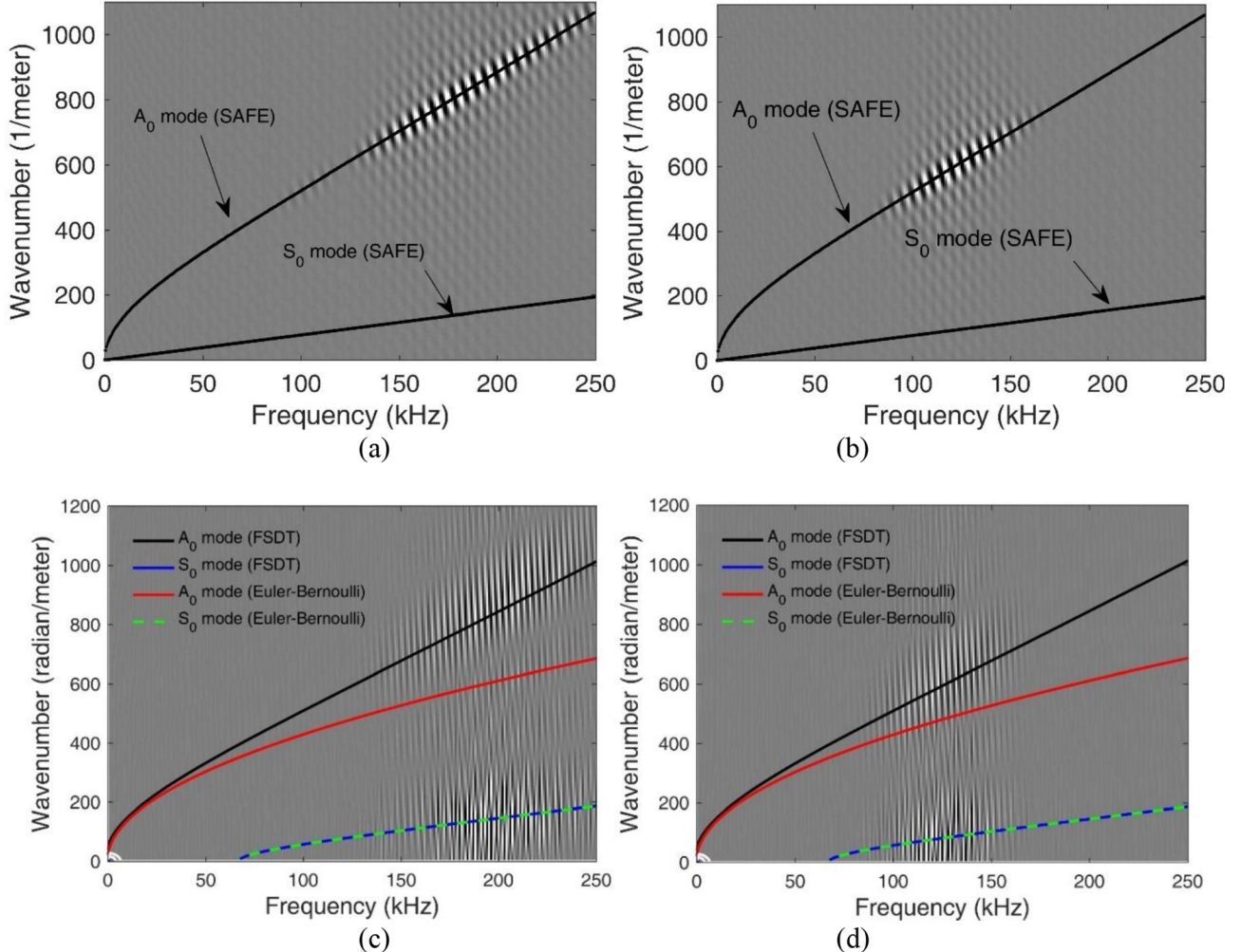


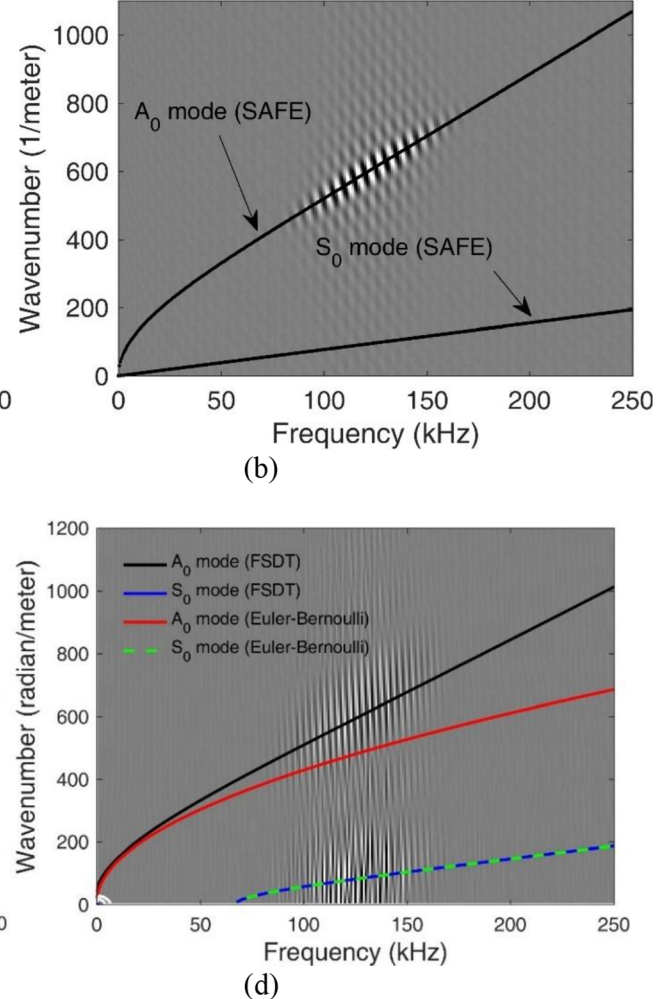
**Fig. 2.** Comparison of dispersion curves obtained from SAFE and with numerical dispersion branches obtained from TSFE simulation for (a) 200 kHz and (b) 125 kHz for flat region, and comparison of dispersion curves obtained from FSDT approximation with numerical dispersion branches obtained from TSFE simulations with excited central frequencies (c) 200 kHz and (d) 125 kHz for curved region.

$$\begin{aligned} \bar{\mathbf{U}}_f^{(p)} &= \begin{bmatrix} u_{11}^{(p)} & u_{12}^{(p)} & u_{13}^{(p)} \\ u_{21}^{(p)} & u_{22}^{(p)} & u_{23}^{(p)} \\ u_{31}^{(p)} & u_{32}^{(p)} & u_{33}^{(p)} \end{bmatrix}, \quad \Lambda_f^{(p)}(y') = \begin{bmatrix} e^{-ik_1^{(p)}y'} & 0 & 0 \\ 0 & e^{-ik_2^{(p)}y'} & 0 \\ 0 & 0 & e^{-ik_3^{(p)}y'} \end{bmatrix}, \quad \mathbf{c}_f^{(p)} \\ &= \begin{bmatrix} c_1^{(p)} \\ c_2^{(p)} \\ c_3^{(p)} \end{bmatrix}, \quad \bar{\mathbf{U}}_b^{(p)} = \begin{bmatrix} u_{14}^{(p)} & u_{15}^{(p)} & u_{16}^{(p)} \\ u_{24}^{(p)} & u_{25}^{(p)} & u_{26}^{(p)} \\ u_{34}^{(p)} & u_{35}^{(p)} & u_{36}^{(p)} \end{bmatrix}, \quad \Lambda_b^{(p)}(y') \\ &= \begin{bmatrix} e^{ik_4^{(p)}y'} & 0 & 0 \\ 0 & e^{ik_5^{(p)}y'} & 0 \\ 0 & 0 & e^{ik_6^{(p)}y'} \end{bmatrix}, \quad \mathbf{c}_b^{(p)} = \begin{bmatrix} c_4^{(p)} \\ c_5^{(p)} \\ c_6^{(p)} \end{bmatrix} \end{aligned}$$

The in-plane longitudinal force, shear force and bending moment are expressed as

$$\begin{aligned} \hat{\mathbf{f}}^{(p)} &= \left\{ \hat{f}_{y'}^{(p)}, \hat{f}_{x'}^{(p)}, \hat{M}'^{(p)} \right\}^T = \hat{\mathbf{f}}_f^{(p)} + \hat{\mathbf{f}}_b^{(p)} = E \bar{\mathbf{U}}_f^{(p)} \Lambda_f^{(p)}(y') \mathbf{c}_f^{(p)} \\ &+ E \bar{\mathbf{U}}_b^{(p)} \Lambda_b^{(p)}(y') \mathbf{c}_b^{(p)} \end{aligned} \quad (40)$$

where



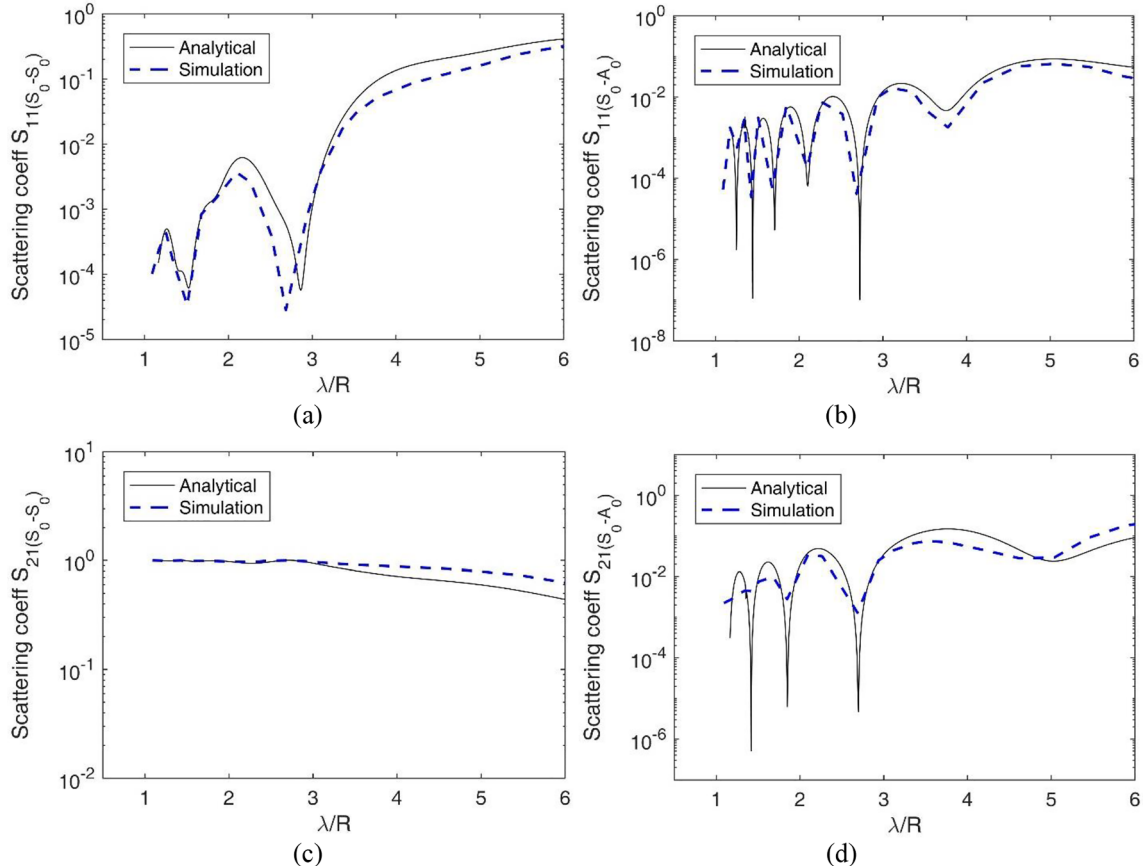


**Fig. 3.** Comparison of scattering coefficients (using Eqs. (52)–(55)) obtained from analytical (FSDT approximation) and simulation (TSFE) for (a) reflected  $S_0$  waves, (b) reflected  $A_0$  waves, (c) transmitted  $S_0$  waves and (d) transmitted  $A_0$  waves due to incident  $S_0$  wave for  $R = 20$  mm and  $h = 1.5$  mm.

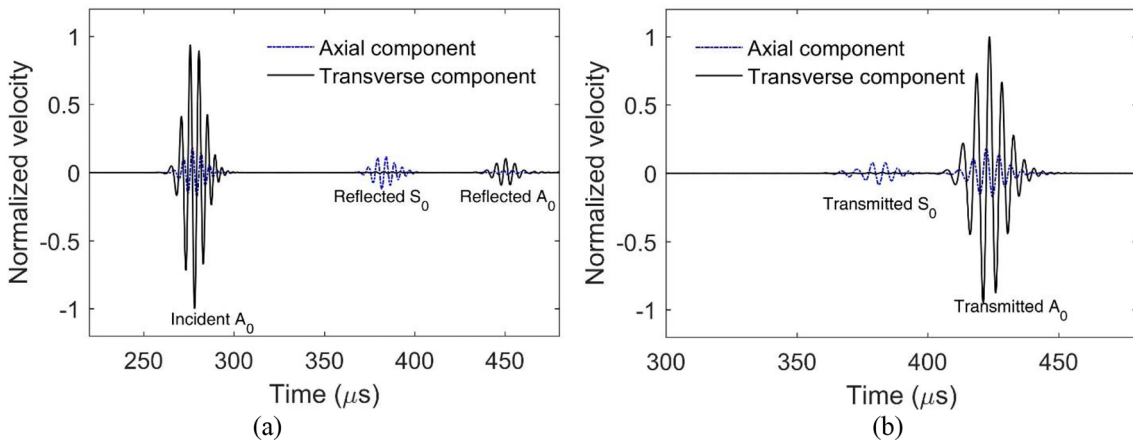


**Fig. 4.** (a) Velocity time history of the incident and reflected waves measured at the point  $T_1$ , (b) velocity time history of the transmitted waves measured at the point  $T_2$  as shown in Fig. 1(b), for  $A_0$  incident waves of carrier frequency 200 kHz.

$$[\tilde{U}_f^{(p)}] = \begin{bmatrix} \frac{U_{21}^{(p)}}{R} + (-ik_1^{(p)}) & \frac{U_{22}^{(p)}}{R} + (-ik_2^{(p)}) & \frac{U_{23}^{(p)}}{R} + (-ik_3^{(p)})U_{13}^{(p)} \\ U_{11}^{(p)} & U_{12}^{(p)} & \\ (-ik_1^{(p)})U_{21}^{(p)} & (-ik_2^{(p)})U_{22}^{(p)} & (-ik_3^{(p)})U_{23}^{(p)} - \frac{U_{13}^{(p)}}{R} \\ -\frac{U_{11}^{(p)}}{R} + U_{31}^{(p)} & -\frac{U_{12}^{(p)}}{R} + U_{32}^{(p)} & + U_{33}^{(p)} \\ (-ik_1^{(p)})U_{31}^{(p)} & (-ik_2^{(p)})U_{32}^{(p)} & (-ik_3^{(p)})U_{33}^{(p)} \end{bmatrix},$$

$$[\tilde{U}_b^{(p)}] = \begin{bmatrix} \frac{U_{24}^{(p)}}{R} + (-ik_4^{(p)})U_{14}^{(p)} & \frac{U_{25}^{(p)}}{R} & \frac{U_{23}^{(p)}}{R} \\ & + (-ik_5^{(p)})U_{15}^{(p)} & + (-ik_6^{(p)})U_{16}^{(p)} \\ (-ik_4^{(p)})U_{24}^{(p)} - \frac{U_{14}^{(p)}}{R} & (-ik_5^{(p)})U_{25}^{(p)} & (-ik_6^{(p)})U_{26}^{(p)} \\ + U_{34}^{(p)} & -\frac{U_{15}^{(p)}}{R} + U_{35}^{(p)} & -\frac{U_{16}^{(p)}}{R} + U_{36}^{(p)} \\ (-ik_4^{(p)})U_{34}^{(p)} & (-ik_5^{(p)})U_{35}^{(p)} & (-ik_6^{(p)})U_{36}^{(p)} \end{bmatrix},$$

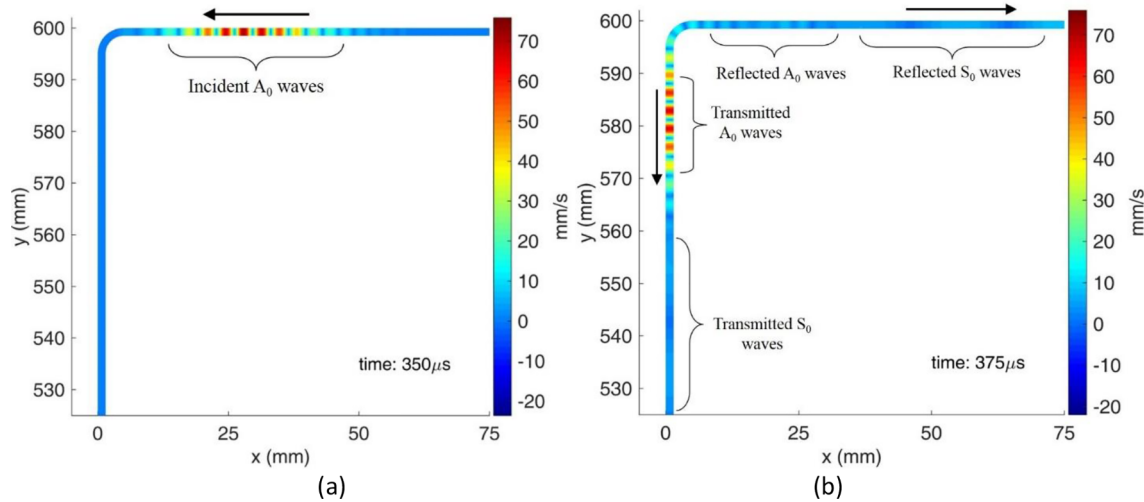


**Fig. 5.** Wave mode conversion in the curved region visualized in terms of total velocity ( $V_{tot} = \sqrt{\dot{u}^2 + \dot{v}^2}$ ) distribution, (a) incident  $A_0$  wave (b) wavefield after interaction with the curved region showing reflected and transmitted waves containing  $S_0$  and  $A_0$  waves.

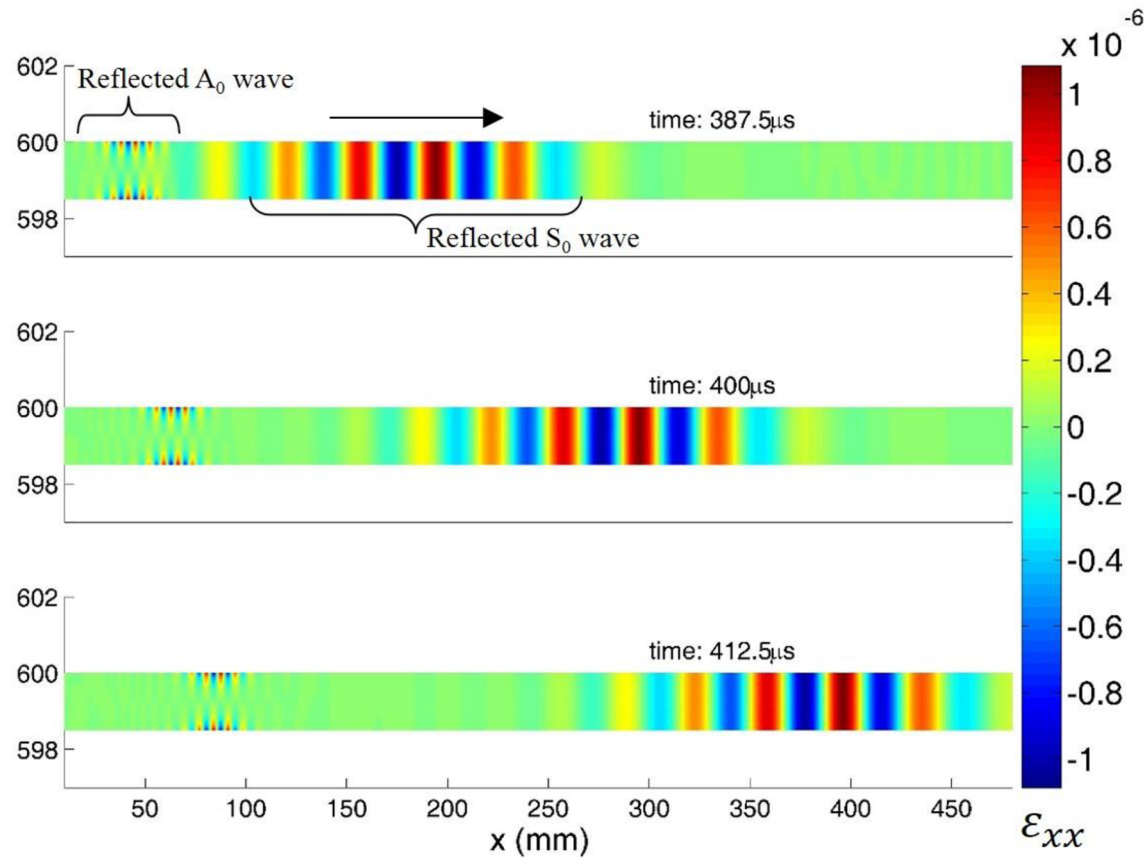


**Fig. 6.** Reflected wave modes with primary  $A_0$  and mode converted  $S_0$  modes after reflection at the curved region (incident segment of the curved region is shown in Fig. 1(b)) visualized in terms axial normal strain ( $\epsilon_{xx}$ ).

$$\mathbf{E} = \begin{bmatrix} A_{11} & 0 & 0 \\ 0 & A_{33} & 0 \\ 0 & 0 & D_{11} \end{bmatrix}$$

There are three sections in the L-segment considered in our presented study. In section-1 and section-2, both the forward and backward propagating waves are present, whereas, in section-3, there are only forward propagating waves as shown in Fig. 1(a). For the complete wavefield, we need to determine 15 coefficients  $c_1^{(p)}, c_2^{(p)}, \dots, c_6^{(p)}$ ,  $p = 1, 2, 3$ . We need 15 boundary conditions to

determine these 15 unknown coefficients. The boundary conditions are as follows, at the port-1 ( $y' = y'_0$ ), displacements and rotation due to forward propagating waves are given as

$$\bar{\mathbf{U}}_f^{(1)} \Lambda_f^{(1)}(y'_0) \mathbf{c}_f^{(1)} = \hat{\mathbf{u}}_I \quad (41)$$

where  $\hat{\mathbf{u}}_I$  is the vector with components of local longitudinal, transverse displacements and rotation angle in the frequency domain due to input incident wave at port-1. At the junction between section-1 and section-2 ( $y' = y'_1$ ), continuity of displacement fields gives

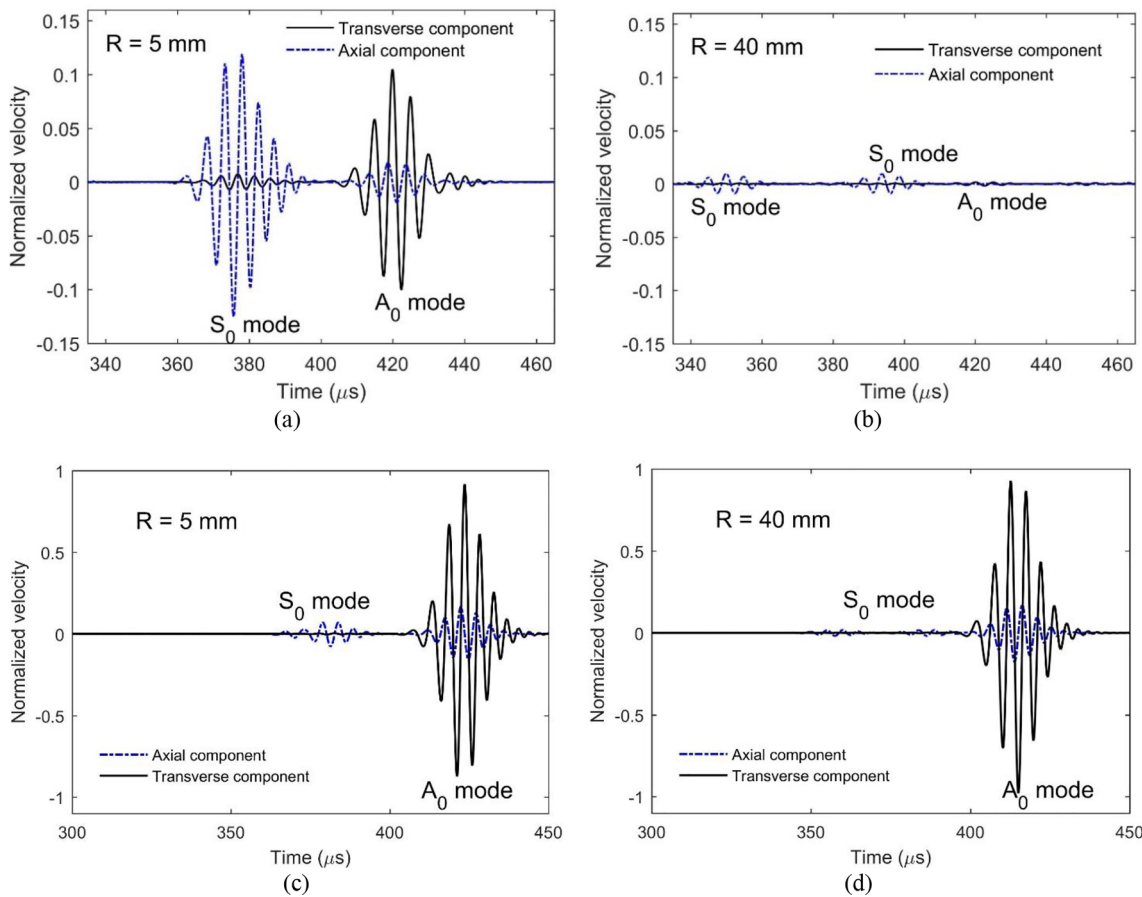


**Fig. 7.** Reflected wave packets from the curved region for radii of curvature—(a) 5 mm, (b) 40 mm, captured at  $T_1$  (Fig. 1(b)) and transmitted wave through curved region for radii of curvature—(c) 5 mm (d) 40 mm, measured at  $T_2$  for incident  $A_0$  wave with central frequency of 200 kHz.

$$\bar{U}_f^{(1)} \Lambda_f^{(1)}(y'_1) \mathbf{c}_f^{(1)} + \bar{U}_b^{(1)} \Lambda_b^{(1)}(y'_1) \mathbf{c}_b^{(1)} = \bar{U}_f^{(2)} \Lambda_f^{(2)}(y'_1) \mathbf{c}_f^{(2)} + \bar{U}_b^{(2)} \Lambda_b^{(2)}(y'_1) \mathbf{c}_b^{(2)} \quad (42)$$

At the junction between section-1 and section-2 ( $y' = y'_1$ ), local longitudinal force, shear force, and bending moment balance give

$$\tilde{U}_f^{(1)} \Lambda_f^{(1)}(y'_1) \mathbf{c}_f^{(1)} + \tilde{U}_b^{(1)} \Lambda_b^{(1)}(y'_1) \mathbf{c}_b^{(1)} = \tilde{U}_f^{(2)} \Lambda_f^{(2)}(y'_1) \mathbf{c}_f^{(2)} + \tilde{U}_b^{(2)} \Lambda_b^{(2)}(y'_1) \mathbf{c}_b^{(2)} \quad (43)$$

At the junction between section-2 and section-3 ( $y' = y'_2$ ), the continuity of displacement fields gives

$$\bar{U}_f^{(2)} \Lambda_f^{(2)}(y'_2) \mathbf{c}_f^{(2)} + \bar{U}_b^{(2)} \Lambda_b^{(2)}(y'_2) \mathbf{c}_b^{(2)} = \bar{U}_f^{(3)} \Lambda_f^{(3)}(y'_2) \mathbf{c}_f^{(3)} + \bar{U}_b^{(3)} \Lambda_b^{(3)}(y'_2) \mathbf{c}_b^{(3)} \quad (44)$$

At the junction between section-2 and section-3 ( $y' = y'_2$ ), the local longitudinal force, shear force, and bending moment balance give

$$\tilde{U}_f^{(2)} \Lambda_f^{(2)}(y'_2) \mathbf{c}_f^{(2)} + \tilde{U}_b^{(2)} \Lambda_b^{(2)}(y'_2) \mathbf{c}_b^{(2)} = \tilde{U}_f^{(3)} \Lambda_f^{(3)}(y'_2) \mathbf{c}_f^{(3)} \quad (45)$$

From the boundary conditions given in Eqs. (41)–(45), all the 15 coefficients are determined. We are interested to calculate the scattering coefficient in terms of power flow. Total power flow due to all propagating waves in section- $p$  of the beam can be written as

$$\hat{P}^{(p)} = (\hat{\mathbf{f}}^{(p)})^H (i\omega \hat{\mathbf{u}}^{(p)}) \quad (46)$$

where  $(\cdot)^H$  denotes Hermitian of a matrix. Power flow due to individual wave modes also can be calculated. Power flow due to  $S_0$  waves is contributed by the axial force and the axial velocity, which can be expressed in the frequency domain as

$$\hat{P}_{S_0}^{(p)} = (\hat{f}_{y'}^{(p)})^* (i\omega \hat{v}_0^{(p)}) \quad (47)$$

where  $(\cdot)^*$  indicates the complex conjugate.  $A_0$  waves cause bending and shearing effect, therefore, power flow caused by  $A_0$  waves is given by

$$\hat{P}_{A_0}^{(p)} = (\hat{f}_{x'}^{(p)})^* (i\omega \hat{u}_0^{(p)}) + (\hat{M}'^{(p)})^* (i\omega \hat{\theta}'^{(p)}) \quad (48)$$

Power flow can be written in terms of scattering coefficients (S matrix).  $S_{ij}$  indicates power outflow at port- $i$  due to incident waves (power inflow) at port- $j$ . If  $\hat{P}_{I1}$  and  $\hat{P}_{I2}$  are power inflow through the port-1 and port-2 respectively, and,  $\hat{P}_{O1}$  and  $\hat{P}_{O2}$  are the power outflow through the port-1 and port-2 respectively, power outflow can be expressed in terms of input power flow using scattering coefficients

$$\begin{bmatrix} \hat{P}_{O1} \\ \hat{P}_{O2} \end{bmatrix} = \begin{bmatrix} S_{11} & S_{12} \\ S_{21} & S_{22} \end{bmatrix} \begin{bmatrix} \hat{P}_{I1} \\ \hat{P}_{I2} \end{bmatrix} \quad (49)$$

In this study, there are input  $S_0$  waves at port-1 and there are no input waves at port-2. Therefore, power outflow can be calculated using  $S_{11}$  and  $S_{21}$ .

$$\begin{bmatrix} \hat{P}_{O1} \\ \hat{P}_{O2} \end{bmatrix} = \begin{bmatrix} S_{11} \\ S_{21} \end{bmatrix} \hat{P}_{I1} \quad (50)$$

Power outflow through port-1 again contributed by reflected  $S_0$  waves and mode converted  $A_0$  waves (reflected)

$$\hat{P}_{O1} = \hat{P}_{O1(S_0)} + \hat{P}_{O1(A_0)} \quad (51)$$

where  $\hat{P}_{O1(S_0)}$  and  $\hat{P}_{O1(A_0)}$  are the power outflow due to reflected  $S_0$  and  $A_0$  waves at port-1. Considering pure  $S_0$  incident waves at port-1,  $\hat{P}_{O1(S_0)}$  and  $\hat{P}_{O1(A_0)}$  can be written as

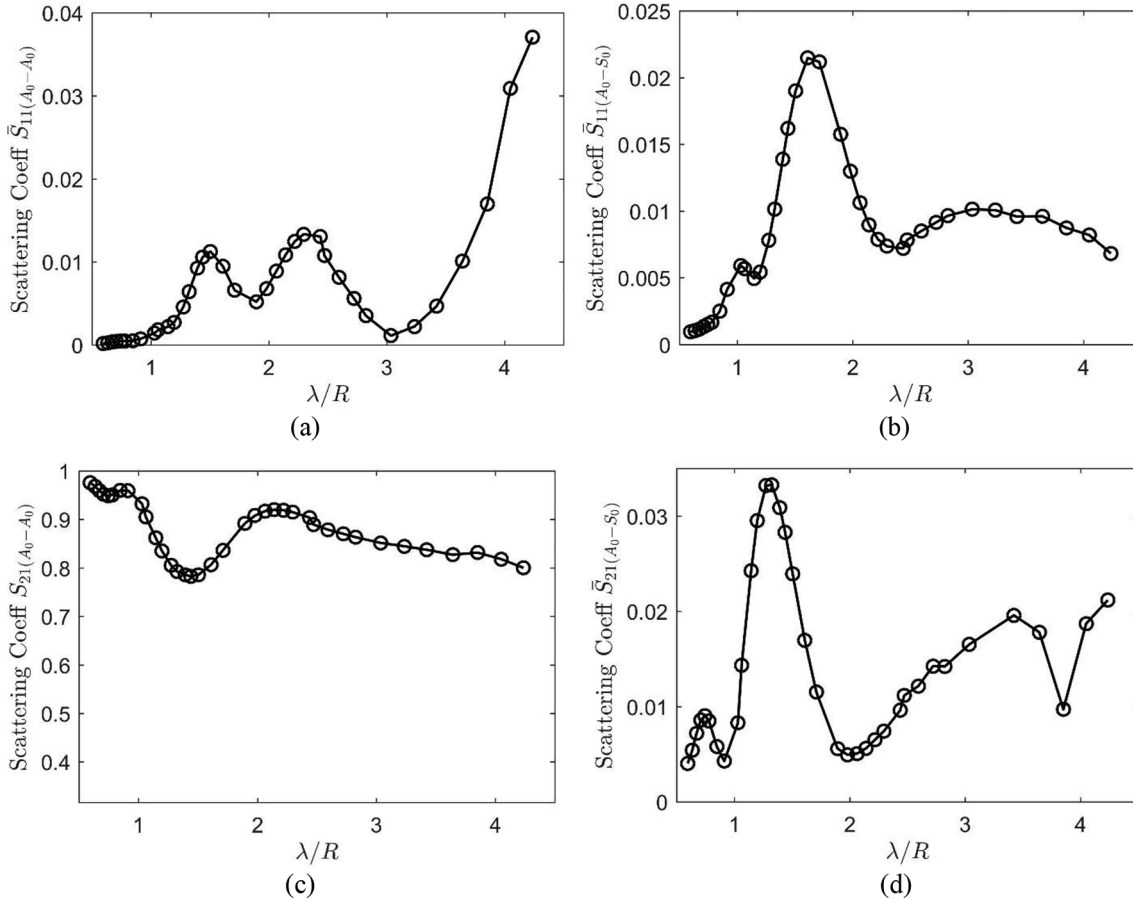


**Fig. 8.** Scattering coefficients (using Eqs. (56)–(58)) for (a) reflected  $A_0$ , (b) reflected  $S_0$  (c) transmitted  $A_0$  and (d) transmitted  $S_0$  at different wave length ( $\lambda$ ) to radius of curvature ( $R$ ) ratio, for incident  $A_0$  waves;  $\lambda$ , the wavelength of incident  $A_0$  waves at horizontal straight section (Fig. 1(b)).

$$\hat{P}_{O1(S_0)} = S_{11(S_0-S_0)} \hat{P}_{I1(S_0)} \quad (52)$$

$$\hat{P}_{O1(A_0)} = S_{11(S_0-A_0)} \hat{P}_{I1(S_0)} \quad (53)$$

Similarly, power outflow at port-2 is caused by transmitted  $S_0$  waves and mode converted  $A_0$  waves (transmitted).  $\hat{P}_{O2(S_0)}$  and  $\hat{P}_{O2(A_0)}$  are written as

$$\hat{P}_{O2(S_0)} = S_{21(S_0-S_0)} \hat{P}_{I1(S_0)} \quad (54)$$

$$\hat{P}_{O2(A_0)} = S_{21(S_0-A_0)} \hat{P}_{I1(S_0)} \quad (55)$$

Above mentioned scattering coefficients  $S_{11(S_0-S_0)}$ ,  $S_{11(S_0-A_0)}$ ,  $S_{21(S_0-S_0)}$  and  $S_{21(S_0-A_0)}$  are estimated from Eqs. (52)–(55) and compared with simulation results in the subsequent sections.

### 2.3. TSFE simulation and analytical results

In this paper, TSFE method is used for simulation of the guided wave propagation in curved laminate with defects. Wavenumber and scattering coefficients at different frequencies obtained from the analytical approach and simulations are considered for comparison.

#### 2.3.1. Wave dispersion behavior

Dispersion relation obtained from TSFE simulation is compared with dispersion relations obtained using analytical methods, FSDT and Euler-Bernoulli beam approximations, and semi semi-analytical finite element (SAFE) method [43]. The analytical dispersion relation is obtained by solving a polynomial eigenvalue problem as given in Eq. (37). The radius of curvature ( $R$ ) is taken as 20 mm and thickness ( $h$ ) is 1.5 mm. A ten layer cross-ply laminate with stacking sequence [(0/

90)<sub>2</sub>/0]<sub>s</sub> is considered. Material properties are given in Table 1. Two cases of dispersion relations, one for the flat region and other for the curved region, are computed. In both cases, a finite number of points in the corresponding region are considered and responses at those points are computed. A 2-D FFT of those spatially varying time signals in frequency-wavenumber space gives numerical dispersion branches. Dispersion relation obtained with this method is in the range of bandwidth of the excitation frequency. Dispersion relations in two different frequency bandwidths with central frequencies of 200 kHz and 125 kHz are shown in Fig. 2. Numerically obtained dispersion branches for flat region is compared with results obtained from SAFE method as shown in Fig. 2(a) and (b), and numerically obtained dispersion branches for curved region are compared with analytical dispersion relation calculated using FSDT and Euler-Bernoulli beam approximation as shown in Fig. 2(c) and (d). Dispersion branches for flat region obtained from TSFE simulation and SAFE method match closely. For the curved region, analytical dispersion relations obtained using Euler-Bernoulli approximation deviates significantly from TSFE simulation. Analytical dispersion from FSDT has smaller difference from TSFE simulation at lower frequency range (125 kHz), but the difference is more at higher frequencies (200 kHz). Substantial discrepancies in the dispersion relations for the curved segment between the numerical results and analytical solutions are because of the approximation errors from both the methods (FSDT and Euler-Bernoulli). Euler-Bernoulli approximations do not consider the shearing effect, and in FSDT approximations, shear stress is considered constant across the thickness, which causes significant approximation error in higher frequencies. In order to obtain numerical dispersion relations using 2-D FFT accurately, it is desired that wave packets move in a particular direction (either forward or backward). The interaction with the curved section creates reflection

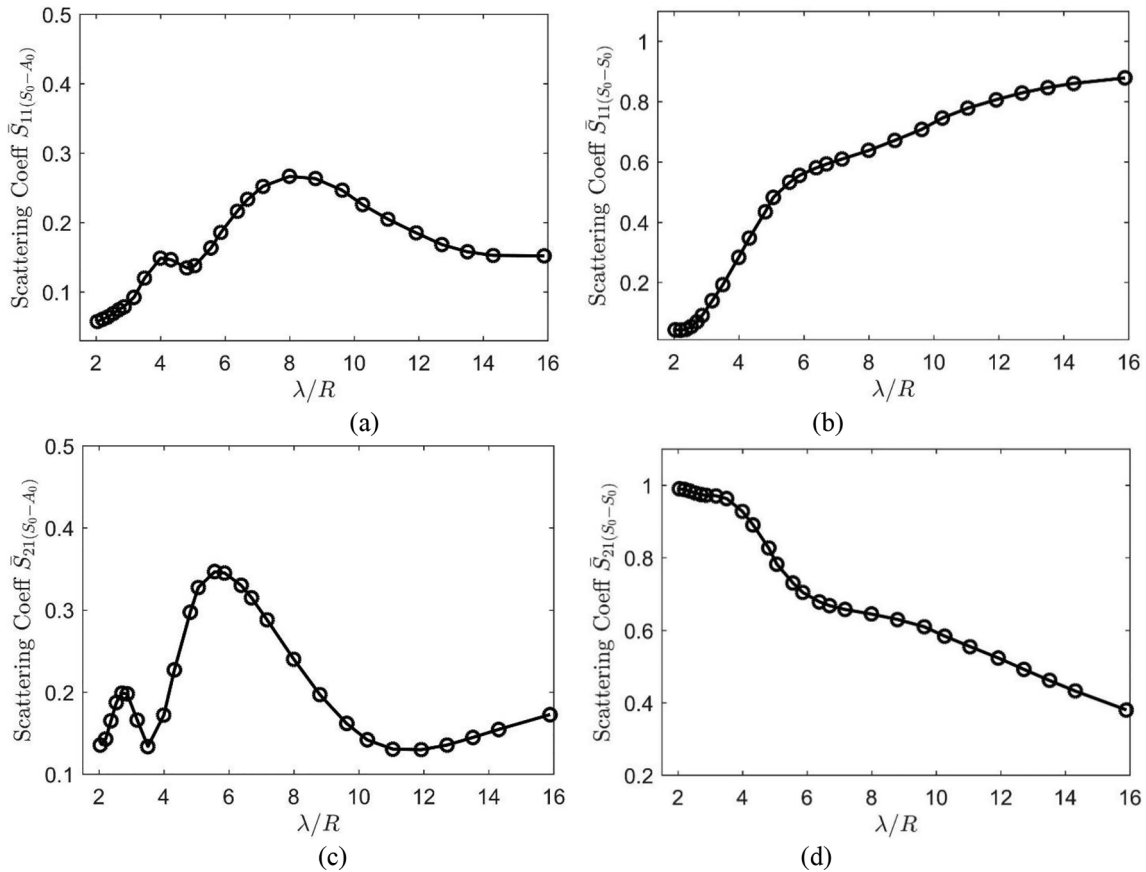


**Fig. 9.** Scattering coefficients (using Eqs. (56)–(58)) for different  $\lambda/R$  for (a) reflected  $A_0$ , (b) reflected  $S_0$ , (c) transmitted  $A_0$  and (d) transmitted  $S_0$  wave, due to incident  $S_0$  waves;  $\lambda$ , the wavelength of incident  $S_0$  waves at horizontal straight section (Fig. 1(b)).

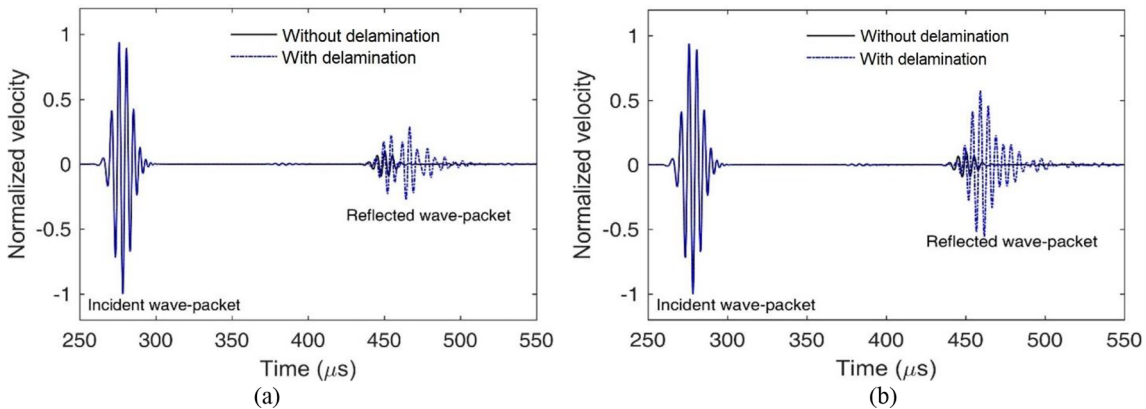


**Fig. 10.** Velocity response for the transverse component from the curved region with delamination at (a) 3rd interface and (b) 5th interface, due to incident  $A_0$  wave of frequency 200 kHz.

and mode conversion in the signal, and both forward and backward propagating waves are present in that segment. It also causes a significant change in the dispersion curve obtained from the TSFE simulation.

### 2.3.2. Scattering coefficients

Wave propagation in the curved structures with a defect is modeled using TSFE and the wave scattering behavior is investigated. Scattering coefficients obtained from TSFE simulation results and FSDT approximation derived in Section 2.2 are compared. Four scattering coefficients obtained from Eqs. (52)–(55) for the L-segment with two end ports are considered for comparison. Fig. 1(b) shows the equivalent structure where the horizontal straight segment is considered section-1,

the curved segment is section-2 and the vertical straight section is considered as section-3. Longer straight segments are taken to eliminate finite boundary scattering in the time domain simulation. The radius of curvature and thickness of the beam are 20 mm and 1.5 mm, respectively. The appropriate converged mesh is considered for TSFE simulation. Longitudinal loading conditions at the end of the straight section creates pure  $S_0$  wave mode. Incident and reflected wave packets are captured at  $T_1$  and transmitted wave packets are captured at  $T_2$  as shown in Fig. 1(b). Power flow is computed from the FFT of generalized force and displacement vectors caused by the incident and reflected wave packets. Scattering coefficients are computed using Eqs. (52)–(55) and the results are compared with the analytical solution (Fig. 3). Overall, results obtained from the analytical model and simulation are

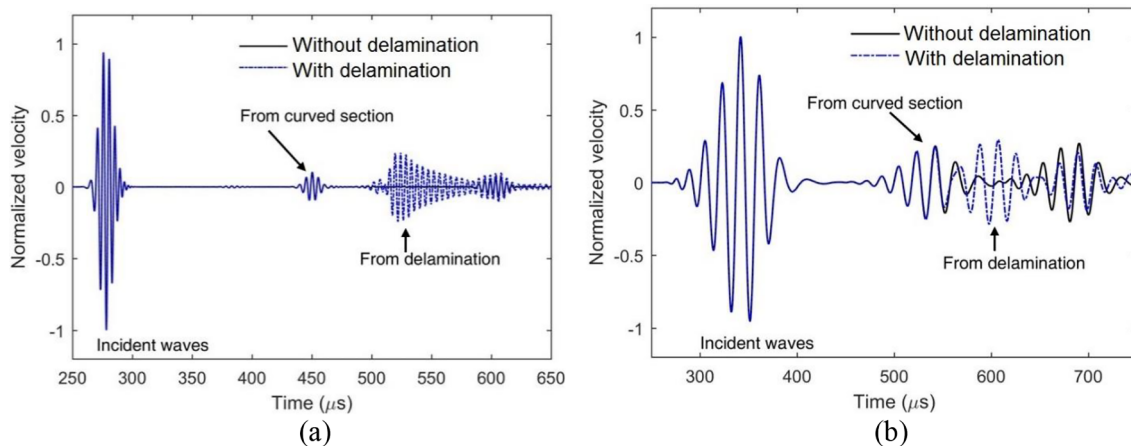


**Fig. 11.** Comparison between responses of the curved beams (radius of curvature of 5 mm) without and with delamination, delamination introduced 50 mm away from the curved region as shown in Fig. 1 (b), and incident A<sub>0</sub> wave frequencies of (a) 250 kHz and (b) 50 kHz.

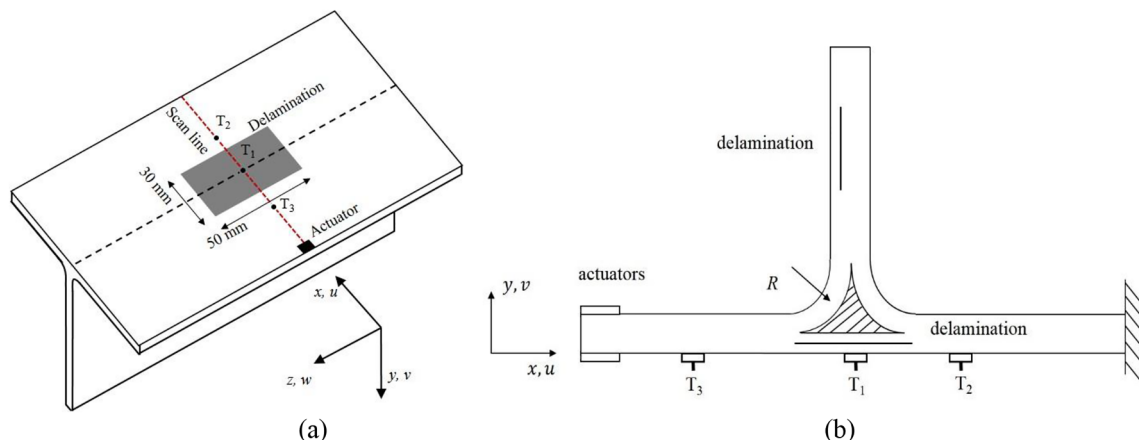


**Fig. 12.** (a) T-Joint with actuator and scan line shown in red dotted line and delamination of size 30 mm  $\times$  50 mm (as shown in gray lines) introduced at the between 3rd and 4th interface counted from the top surface, (b) Schematic composite T-Joint (cross-sectional cut view w.r.t dashed red line shown in 3D view) with delamination located below the joint and the gap shown in the marked area filled with epoxy.

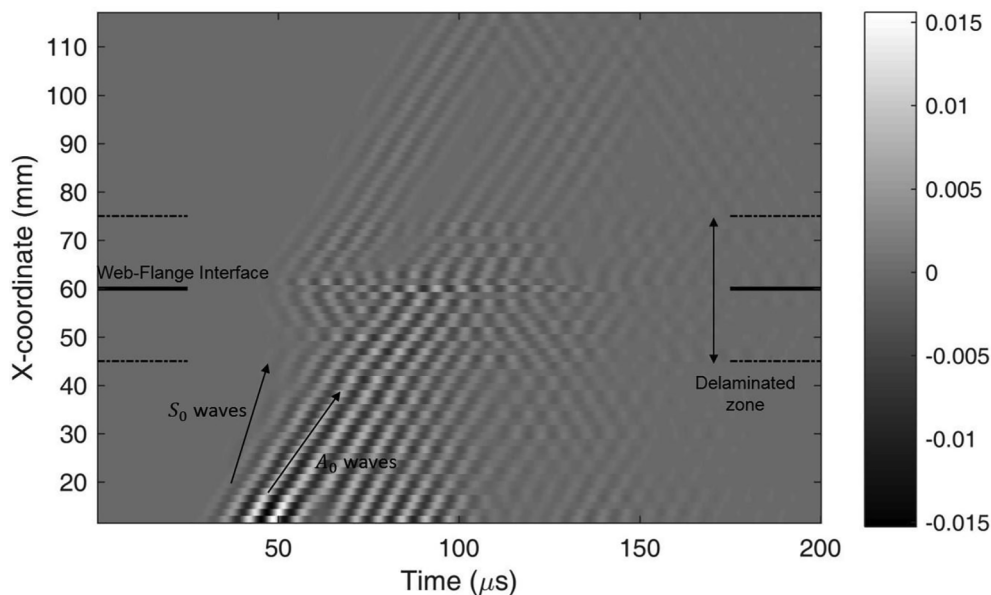


**Fig. 13.** B-scan image for LDV line scan (as marked in Fig. 12).

**Table 2**

Material properties of the composite T-joint.

$E_{11}$ (GPa)	$E_{22}, E_{22}$ (GPa)	$G_{12}, G_{13}$ (GPa)	$G_{23}$ (GPa)	$\nu_{12}, \nu_{13}$	$\rho$ (kg/m <sup>3</sup> )
30.8	7.27	4.14	2.7	0.3	2280

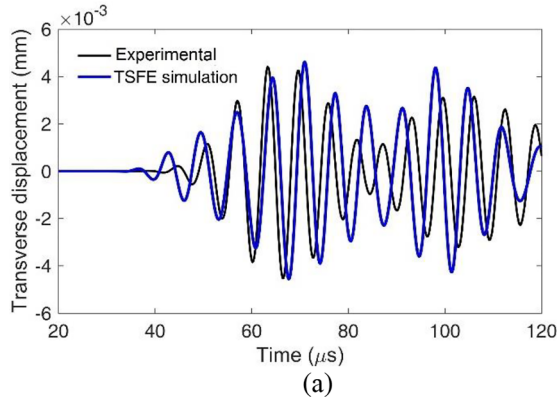
in good agreement. It is observed that at high frequencies most of the energy is transmitted without much mode conversion or reflection. At lower wavelength (high frequency), both analytical and simulation results match closely. There is a deviation in scattering parameters associated with transmitted and mode converted waves with TSFE simulation when wavelength becomes longer, again at very high-frequency FSDT approximation induce error due to inaccurate shear. Therefore, finite element-based simulation is required to get solutions with higher accuracy in wider frequency range.

### 3. Guided wave propagation in a curved composite

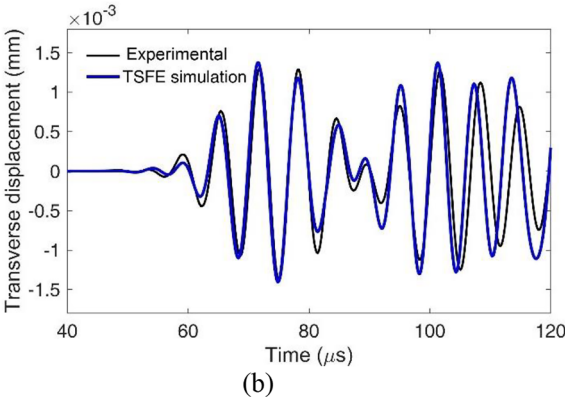
Guided wave interaction with a curved section creates reflection and transmission of primary wave modes along with additional wave modes due to mode conversion of the incident wave during propagation through the curved region. For amplification of wave scattering from defect located in the curved region, maximum transmission of wave mode at the entry section of the curved part is desired, and similarly, maximum reflection from the defect must get transmitted back through the curved region. Therefore, quantification of signal loss and uncorrelated signal or noise caused by wave scattering and mode conversions due to curvature for different frequencies are important aspects studied here. The curved segment (Fig. 1(b)) has a constant radius of curvature. Lengths of both the horizontal and vertical straight segments are taken as 600 mm. Material properties and stacking of composite laminate are taken same as in the previous section. The actuators are operated in or out of phase to achieve symmetric ( $S_0$ ) or anti-symmetric wave mode ( $A_0$ ), respectively. Hanning windowed narrow-band signal is applied as excitation to the actuators, the frequency content of the signal is shown in Fig. 1(b). Two sensor locations  $T_1$  and  $T_2$  are considered for collecting reflected and transmitted signals from the horizontal and vertical sections, respectively.

#### 3.1. Wave mode conversion in the curved region

Fundamental anti-symmetric (flexural) wave mode ( $A_0$ ) is sensitive to small change or defect that breaks the anti-symmetry of displacement field across the thickness (for defects located away from the neutral plane). The curved geometry causes the breaking of symmetry or anti-symmetry along the propagation path. For the  $A_0$  wave excited from the actuators, the response captured at  $T_1$  and  $T_2$  are plotted in Fig. 4(a) and (b), respectively. Longitudinal and transverse components of



(a)



(b)

Fig. 14. Comparison of transverse velocity responses obtained from experiments and TSFE simulation measured at (a) point  $T_1$  and (b) point  $T_2$  as shown in Fig. 12.

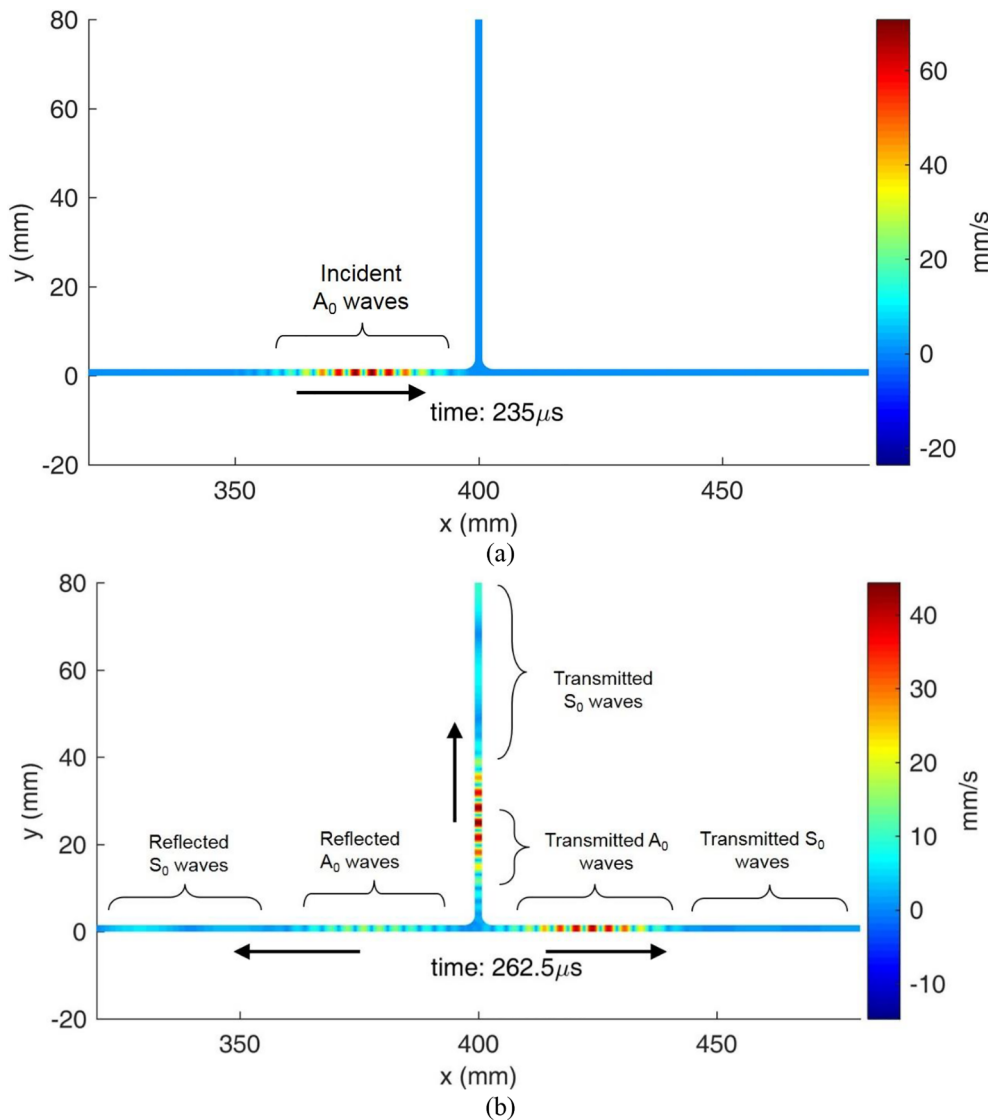


**Fig. 15.** Visualization of the wavefield in terms of total velocity distribution for (a) Incident wave field and (b) wavefield after the interaction.

superscripts,  $I$ ,  $R$  and  $T$  correspond to the incident, reflected and transmitted waves, respectively. In our present study, incident waves enter through port-1 and there are no incidents waves enter through port-2. Therefore, we are interested to calculate two scattering parameters  $\bar{S}_{11}$  and  $\bar{S}_{21}$ . Scattering coefficients in terms of signal energy are calculated as

$$\begin{aligned} \bar{S}_{11(A_0-A_0)} &= \frac{E_{1(A_0)}^{(R)}}{E_{1(A_0)}^{(I)}}, & \bar{S}_{11(A_0-S_0)} &= \frac{E_{1(S_0)}^{(R)}}{E_{1(A_0)}^{(I)}}, & \bar{S}_{11(S_0-S_0)} \\ &= \frac{E_{1(S_0)}^{(R)}}{E_{1(S_0)}^{(I)}}, & \bar{S}_{11(S_0-A_0)} &= \frac{E_{1(A_0)}^{(R)}}{E_{1(S_0)}^{(I)}} \end{aligned} \quad (57)$$

$$\begin{aligned} \bar{S}_{21(A_0-A_0)} &= \frac{E_{2(A_0)}^{(T)}}{E_{1(A_0)}^{(I)}}, & \bar{S}_{21(A_0-S_0)} &= \frac{E_{2(S_0)}^{(T)}}{E_{1(A_0)}^{(I)}}, & \bar{S}_{21(S_0-S_0)} \\ &= \frac{E_{2(S_0)}^{(T)}}{E_{1(S_0)}^{(I)}}, & \bar{S}_{21(S_0-A_0)} &= \frac{E_{2(A_0)}^{(T)}}{E_{1(S_0)}^{(I)}} \end{aligned} \quad (58)$$

Using these defined quantities as given in Eqs. (56)–(58), effects of frequency on signal strength of reflected and mode converted waves are investigated. For an L-shaped curved laminate, a curved region of 10 mm radius of curvature is considered for simulation. Fundamental

antisymmetric ( $A_0$ ) or symmetric ( $S_0$ ) wave mode is considered as primary incident wave mode. The structure is excited at a number of frequencies in the range of 50 kHz to 250 kHz. Responses are captured for all excited frequencies and scattering coefficients are calculated for each frequency. Scattering coefficients for various ratios of wavelength to radius of curvature ( $\lambda/R$ ) are plotted in Figs. 8 and 9 for incident  $A_0$  waves and  $S_0$  waves, respectively.  $\lambda$  is the wavelength of corresponding primary incident wave mode. Both the incident wave modes cause mode conversions, which are present in reflected as well as transmitted waves. In the plot, it can be seen that for smaller  $\lambda/R$ , scattering coefficients for mode converted waves as well as reflected waves are very small indicating that below a certain wavelength that is above a certain frequency, there is the only transmission without much mode conversions. Wave transmission through the curved region is not varying in a similar manner. At some frequencies, there is a significant amount of signal loss due to reflection and mode conversion. Therefore it is intuitive that defect identification cannot be performed in those frequency ranges. Mode conversion from  $S_0$  waves creates high amplitude  $A_0$  waves. From Fig. 9 it is observed that scattering coefficients of mode converted waves due to incident  $S_0$  wave is significantly high. It is because axial stiffness is very high compared to the flexural rigidity of the laminate.  $S_0$  wave has longer wavelengths comparison to the  $A_0$  waves in the given operating frequency range. Therefore, wave packet

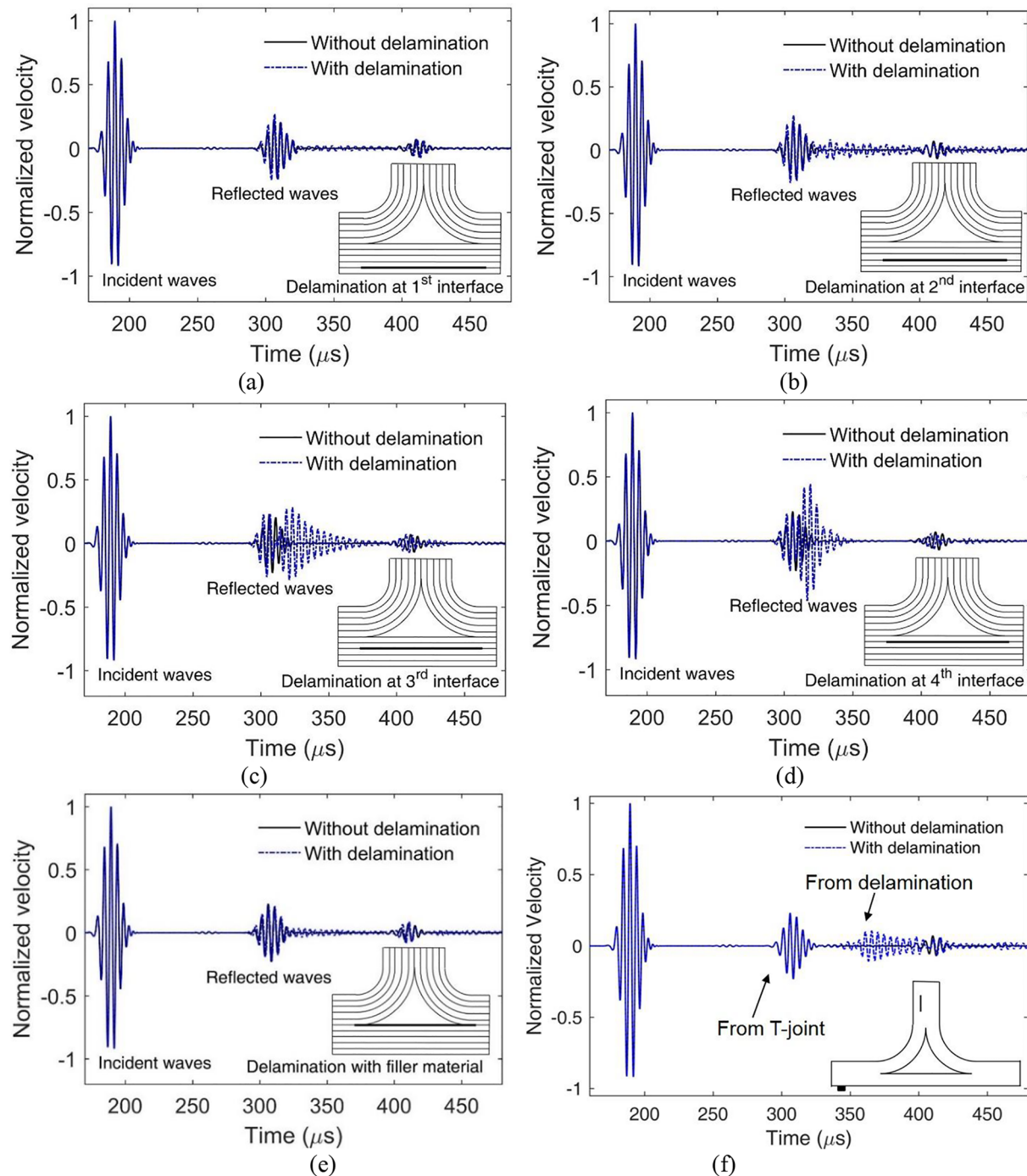


**Fig. 16.** Transverse velocity responses measured at  $T_3$  for different delamination at (a) 1<sup>st</sup> (b) 2<sup>nd</sup> (c) 3<sup>rd</sup> (d) 4<sup>th</sup> interface and (e) adjacent layer with radius filler for excitation frequency 200 kHz, (f) velocity response captured at  $T_3$  for the cases without and with delamination at the web of T-joint as shown in the Fig. 12 (b).

energy of  $S_0$  wave mode spread over larger region comparative to  $A_0$  wave mode. When a part of incident  $S_0$  wave converted into  $A_0$  wave, mode converted wave energy is concentrated in the smaller region, which led to higher amplitude. So, using  $S_0$  wave mode as the inspection wave mode creates more signal noise due to mode conversion. Moreover,  $S_0$  wave mode has a higher wavelength than that of  $A_0$  wave mode. In the inspection of the structure with the curved region,  $A_0$  wave mode has better effectiveness comparative to  $S_0$  wave mode.

### 3.3. Wave scattering from delamination in the curved region

As discussed in the previous section from the scattering coefficient

plot that  $A_0$  would be preferable for defect inspection in a structure with curvature.  $A_0$  waves have a shorter wavelength compared to the wavelength of  $S_0$  waves in a similar frequency range. Shorter wavelength has higher transmissibility. So, most of the  $A_0$  waves are transmitted without much reflection and mode conversions compared to the  $S_0$  waves. Here two cases have been studied, in one case delamination is in the curved section and in the other case delamination is beyond the curved section. For delamination in the curved region, two cases are considered. In one case, delamination is introduced at mid-plane (5<sup>th</sup> interface) and in another case, delamination is introduced at the third interface. The radius of curvature is 10 mm and the frequency of exciting  $A_0$  wave mode is considered to be 200 kHz. Responses are

captured at  $T_1$  (as shown in Fig. 1(b)) and plotted in Fig. 10. In both cases,  $A_0$  wave is able to bring the damage induced responses. Reflection from the defect is significantly stronger than the reflection due to the curvature effect. Noticeable difference in responses is observed between responses from the curved section with delamination and without delamination.

In many practical problems, for a structural component with a curved section, one part is accessible, but other part may not be accessible. Accessible part may be inspected using local methods; however, guided wave-based inspection methods are suitable for inspection of the inaccessible part. In this study, L-joint with delamination is modeled. The actuator is mounted at the tip of the horizontal section from where the waves are generated and the delamination is introduced at the vertical part of the beam as shown in Fig. 1(b), considering vertical part as inaccessible part. Two different frequencies are considered— one is in the high-frequency zone of 250 kHz and another one is in a lower frequency zone that is 50 kHz. In transverse velocity response for the case when delamination is present, an additional wave packet appears in the plot as shown in Fig. 11, which is the reflection from the delamination. The position of the delamination can be estimated from the time of flight of the reflected wave packet. For high frequency (250 kHz), wave response from the defect is identified, where the reflection from the curved section and the defect is well separated. For high frequency, wave packet spread is less compared to the low-frequency excitation as shown in Fig. 11, and the high-frequency waves reflect less energy from the curved section. For high frequency (250 kHz) waves, defect response is clearly identified compared to the other case. So, in order to inspect the inaccessible part of the curved structural component, high-frequency waves are more advantageous. Moreover, the high-frequency waves have higher transmissibility; therefore, the signal loss is less, again defect induced signal also passes back without much signal loss. In high frequency, the signal length will be shorter and there is less possibility of overlapping between the incident and reflected wave packets.

#### 4. Guided wave scattering due to delaminated composite T-joint

Wave propagation in composite T-joint is studied using TSFE simulation. We consider a composite T-joint as shown in Fig. 12(b) for simulation. For validation of the TSFE simulation, the response is compared with Laser Doppler vibrometer (LDV) scan result. In the TSFE simulation, we simplified the model using 2-D plane strain assumptions, which captures the displacement field in the sagittal plane for far-field waves. For this study, we consider a composite T-Joint sample [23] with dimensions as follows: 300 mm length, 125 mm flange and 100 mm web. The laminate has 8 layers and stacking sequences are as follows: (90/45/-45/0)<sub>8</sub>. The thickness of each layer is 0.25 mm. Material properties of the laminate are given in Table 2. A square actuator is mounted at one of the edges of flange and LDV scan is performed along the line marked in red color as shown in Fig. 12(a). For TSFE simulation, we considered the 2-D domain which is formed due to the cut by the plane parallel to x-y plane passing through the red dotted line as shown in Fig. 12. In the thickness direction, each layer is modeled using one element and in the direction of propagation at least 8 elements are considered for a wavelength. The actuator is excited with 5 cycle Hanning windowed sinusoidal pulse at the central frequency of 150 kHz. The actuator is mounted at one surface, therefore, both  $S_0$  and  $A_0$  wave modes are generated from the actuator. Actuators are mounted at the edge and the size of the actuator is small compared to the wavelength, so there is no significant time gap between the actuator signal and reflection from the edge. Therefore, distinct wave packets due to the edge reflection are not created. Velocity responses (transverse) at two points are compared with simulation results as shown in Fig. 14 and the B-scan image is plotted in Fig. 13. In B-scan, we can see that the reflection and mode conversions take place from the delamination as well as the joint.  $S_0$  wave mode travels faster than the  $A_0$  wave mode as

$S_0$  wave mode has higher velocity.

Because of mode conversions and reflections, multiple wave packets appear, and overlapping takes place. Therefore, a specific wave packet cannot be distinguished separately. Displacement responses in the y-direction are compared between simulation and experimental results. For comparison of the responses obtained from LDV scan and TSFE simulation, responses are scaled to match the incident wave packet amplitude. Responses are plotted in Fig. 14(a) and (b) for two points at  $T_1$  and  $T_2$  respectively. Point  $T_1$  is located in the middle of the plate and  $T_2$  is located behind the delamination tip as shown in Fig. 12. For each case, the incident wave packet is normalized with the appropriate factor. In Fig. 14, first wave packets are the incident  $A_0$  wave packets and subsequent wave packets are due to the wave interaction between joint and delamination. Trailing wave packets have lower amplitudes in the experiment compared to simulation results obtained from 2-D approximation because of significant cylindrical loss occurred due to the small size of the sample. In subsequent simulations, we consider that actuators are mounted far away from the region of inspection, which will ensure the minimal cylindrical loss due to propagation.

$A_0$  wave mode interaction with T-joint with delamination simulated using TSFE. A 10-layer T-shaped composite structure is considered, the total length of the horizontal section is 800 mm and the vertical section has a length of 400 mm. Laminate material properties are given in Table 1 and stacking sequences are taken the same as in Section 2.3.1. The vertical section meets in the middle of the horizontal section as shown in Fig. 12(b). The gap created by the joint is filled with fiber and epoxy. Material properties of the filler region are given in Table 3. The radius of curvature ( $R$ ) near the T-joint region is considered as 5 mm. Waves are generated from the leftmost part of the horizontal section. The rightmost part of the horizontal section is fixed to restrict rigid-body motion. In one case of the study, wave propagation is studied without delamination in the structure. Wavefield is visualized in terms of total velocity in Fig. 15. Waves generated from the tip travel through the horizontal section. After interaction with joint, part of the energy is transmitted to the web and right part of the flange, and some part is reflected back.

In a realistic case, there can be multiple delaminations in the base of the T-joint due to a bending load. Dealing with such complicated damage configuration is beyond the scope of this study. Single delamination is considered in this study to simplify the problem. Single delamination is introduced at the base of the T-joint for the different interface of the laminate. The length of the delamination considered 8 mm and extended symmetrically both side of the joint. The delamination interface position varies from the bottom interface to the filler gap. Composite T-joint is inspected using  $A_0$  waves and responses are plotted for different cases of delamination positions in the base region of T-joint. Responses measured at point  $T_3$  are plotted in Fig. 16.  $T_3$  is located at 300 mm away measured from the tip where actuators are mounted. In some interface position, reflection from the delamination can be identified properly as in cases when delamination is in 3<sup>rd</sup> or 4<sup>th</sup> interfaces. In Fig. 16(c) and (d) defect response is delayed compared to the response from the joint. It is because delamination scattering happens predominantly from the trailing delamination tip. The crack between lower laminate and filler material in the triangular region creates very less amount of reflection compared to the interlaminar debonding. The material stiffness of filler material is very less compared to that of laminate resulting in no significant change in signal as shown in Fig. 16(e). A distinct wave packet is observed when delamination is interior to the laminate. In the case of delamination is near the surface, instead of separable wave packets, it creates a continuous low amplitude signal due to the reverberation of the thinner sub-laminate.

Web of T-joint structure may be inaccessible and inspection can be performed using guided waves. One case of simulation is performed to show the ability of guided waves to capture defect signature from the inaccessible part in T-joint. Delamination of length 8 mm is introduced at the web at the distance of 50 mm from joint as shown in Fig. 12(b).

Material properties of laminate are given in [Table 1](#) and properties of filler material are given in [Table 3](#). Antisymmetric wave mode at 200 kHz is used and response is captured at T<sub>3</sub> as shown in the simulation set up in [Fig. 12\(b\)](#). The responses are plotted in [Fig. 16\(f\)](#). A distinct wave packet is identified in the response, which is due to the wave interaction with the defect located in the web.

## 5. Conclusions

Multilayered composite with a curved section is modeled using TSFE to study the wave scattering behavior due to wave interaction with the curved region. The effects of curvature on dispersion and mode conversions are studied with the help of simulation and analytical results. Dispersion relation and scattering coefficients due to curvature effect obtained from analytical model and simulations are overall in good agreement. For curved structures, at lower frequencies that is when wavelength is longer, analytical model gives more error. Again, analytical models based on Euler-Bernoulli or FSDT induce large error which causes erroneous prediction in wave responses at higher frequencies. Therefore, FE simulation is advantageous to obtain accurate responses in wider frequencies, especially for curved structures. Reflection, transmission and mode conversion due to A<sub>0</sub> and S<sub>0</sub> wave interaction is correlated with the ratio of wavelength to the radius of curvature. Wave scattering due to interaction with a curved section and its propagation are visualized in terms of strain and velocity distributions. Loss in signal strength due to reflection and mode conversion depends on wavelength to the radius of curvature ratio. The signal strength of mode conversions and reflection is reduced at a shorter wavelength and most of the energies are then transmitted. S<sub>0</sub> wave has a longer wavelength than that of the A<sub>0</sub> wave. Moreover, mode conversion due to incident S<sub>0</sub> wave mode interaction creates a stronger signal of A<sub>0</sub> wave mode comparative to the otherwise case. Therefore, A<sub>0</sub> wave mode is more preferable to interrogate defects in a curved structure. High-frequency waves cause high transmissions and low energy loss, and at high frequency, wave packet spread becomes shorter, which reduces the possibility of overlap between the incident and reflected wave signals. High-frequency waves are more effective for inspection of structure with curvature. Defect response from the inaccessible part of the structure using A<sub>0</sub> wave excitation is identified, which will be helpful towards the development of detection algorithm in structures with curved geometry. The distinct feature of reflected response from delamination at the base of the T-joint is observed when the defect is near the surface. It reflects low amplitude continuous signal due to reverberation after waves pass the T-joint. The reverberation of the sub-laminate can be observed using ultrasonic imaging-based technique, which is future scope of this study.

## CRediT authorship contribution statement

**Rajendra Kumar Munian:** Conceptualization, Methodology, Writing - original draft, Software, Validation, Writing - review & editing, Data curation. **D. Roy Mahapatra:** Conceptualization, Formal analysis, Resources, Validation, Writing - review & editing, Supervision. **S. Gopalakrishnan:** . : Resources.

## Declaration of Competing Interest

The authors declare that they have no known competing financial interests or personal relationships that could have appeared to influence the work reported in this paper.

## Acknowledgements

Authors gratefully acknowledge the help of Dr Ganesh Kolappan Geetha in generating experimental data from LDV scan of T-joint.

## References

- [1] Giurgiutiu V, Bao J, Zhao W. Piezoelectric wafer active sensor embedded ultrasonics in beams and plates. *Exp Mech* 2003;43(4).
- [2] Zhao G, Wang B, Wang T, Hao W, Luo Y. Detection and monitoring of delamination in composite laminates using ultrasonic guided wave. *Compos Struct* 2019;225(June):111161.
- [3] Kessler SS, Spearing SM, Soutis C. Damage detection in composite materials using Lamb wave methods. *Smart Mater Struct* 2002;11(2):269–78.
- [4] Alleyne DN, Lowe MJS, Cawley P. The reflection of guided waves from circumferential notches in pipes. *J Appl Mech* 1998;65(3):635–41.
- [5] Demma A, Cawley P, Lowe M, Roosenbrand AG, Pavlakovic B. The reflection of guided waves from notches in pipes: a guide for interpreting corrosion measurements. *NDT E Int* 2004;37(3):167–80.
- [6] Hinders MK, Bingham JP. Lamb wave pipe coating disbond detection using the dynamic wavelet fingerprinting technique. *AIP Conf Proc* 2010;1211(1):615–22.
- [7] Gresil M, Poohsai A, Chandarana N. Guided wave propagation and damage detection in composite pipes using piezoelectric sensors. *Procedia Eng* 2017;188:148–55.
- [8] Seeger J, Wolf K. Multi-objective design of complex aircraft structures using evolutionary algorithms. *Proc Inst Mech Eng Part G J Aerosp Eng* 2011;225(10):1153–64.
- [9] Hunten KA, Barnard A, Srinivasan V. Computer-aided design recent advances in sharing standardized STEP composite structure design and manufacturing information. *Comput Des* 2013;45(10):1215–21.
- [10] Schmidt H, Schmidt-brändlecker B. Damage tolerant design and analysis of current and future aircraft structures. In: AIAA international air and space symposium and exposition: the next 100 years; 2003, p. 2784.
- [11] Demma A, Cawley P, Lowe MJS. Mode conversion of longitudinal and torsional guided modes due to pipe bends. *AIP Conf Proc* 2001;557:172–9.
- [12] Nishino H, Yoshida K, Cho H, Takemoto M. Propagation phenomena of wideband guided waves in a bended pipe. *Ultrasonics* 2006;44:e1139–43.
- [13] Yashiro S, Takatsubo J, Miyauchi H, Toyama N. A novel technique for visualizing ultrasonic waves in general solid media by pulsed laser scan. *NDT&E Int* 2008;41(2):137–44.
- [14] Qi MX, Zhang PG, Ni J, Zhou SP. Experiment and numerical simulation of ultrasonic guided wave propagation in bent pipe. *Procedia Eng* 2015;130:1603–11.
- [15] Janarthan B, Mitra M, Mujumdar PM. Damage detection in stiffened composite panels using lamb wave. In: 6th European workshop on structural health monitoring; 2012.
- [16] Chetwynd D, Mustapha F, Worden K, Rongrong JA, Pierce SG. Damage localisation in a stiffened composite panel. *Strain* 2008;24(4):298–307.
- [17] Wang JT, Ross RW, Huang GL, Yuan FG. Simulation of detecting damage in composite stiffened panel using lamb waves. 2013.
- [18] Roy Mahapatra D, Gopalakrishnan S, Sankar TS. Spectral-element-based solutions for wave propagation analysis of multiply connected unsymmetric laminated composite beams. *J Sound Vib* 2000;237(5):819–36.
- [19] De Luca A, Perfetto D, De Fenza A, Petrone G, Caputo F. Guided waves in a composite winglet structure: numerical and experimental investigations. *Compos Struct* 2019;210(November 2018):96–108.
- [20] Ramadas C, Balasubramanian K, Joshi M, Krishnamurthy CV. Interaction of Lamb mode (A<sub>0</sub>) with structural discontinuity and generation of “Turning modes” in a T-joint. *Ultrasonics* 2011;51(5):586–95.
- [21] Trask RS, Hallett SR, Helenon FMM, Wisnom MR. Influence of process induced defects on the failure of composite T-joint specimens. *Composites* 2012;43(4):748–57.
- [22] Chuyang LUO, Junjiang X. Static pull and push bending properties of RTM-made TWF composite tee-joints. *Chin J Aeronaut* 2012;25(2):198–207.
- [23] Geetha GK, Mahapatra DR, Gopalakrishnan S, Hanagud S. Laser Doppler imaging of delamination in a composite T-joint with remotely located ultrasonic actuators. *Compos Struct* 2016;147:197–210.
- [24] Ramadas C, Balasubramanian K, Joshi M, Krishnamurthy CV. Sizing of interface delamination in a composite T-joint using time-of-flight of lamb waves. *J Intell Mater Syst Struct* 2011;22(8):757–68.
- [25] Apalowo RK, Chronopoulos D. A wave-based numerical scheme for damage detection and identification in two-dimensional composite structures. *Compos Struct* 2019;214(November 2018):164–82.
- [26] Philibert M, Soutis C, Gresil M, Yao K. Damage detection in a composite T-joint using guided lamb waves. *Aerospace* 2018;5(2):40.
- [27] Morley LSD. Elastic waves in a naturally curved rod. *Q J Mech Appl Math* 1961;14(2):155–72.
- [28] Crowley FB, Phillips JW, Taylor CE. Pulse propagation in straight and curved beams-theory and experiment. *J Appl Mech* 1974;41(1):71–6.
- [29] Doyle JF. Wave propagation in structures. 1st ed. New York: Springer-Verlag; 1989.
- [30] Graff KF. Wave propagation in a curved sonic transmission line. *IEEE Trans Sonic Ultrason* 1970;17(1):1–6.
- [31] Graff KF. Wave motion in elastic solids. Courier Corporation; 2012.
- [32] Treyyssède F. Mode propagation in curved waveguides and scattering by inhomogeneities: application to the elastodynamics of helical structures. *J Acoust Soc Am* 2011;129(4):1857–68.
- [33] Chakraborty A, Roy Mahapatra D, Gopalakrishnan S. Finite element analysis of free vibration and wave propagation in asymmetric composite beams with structural discontinuities. *Compos Struct* 2002;55(1):23–36.
- [34] Mahapatra DR, Gopalakrishnan S. A spectral finite element for analysis of wave propagation in uniform composite tubes. 2003;268.
- [35] Nanda N, Kapuria S. Spectral finite element for wave propagation in curved beams.

- J Vib Acoust 2015;137(4):41005.
- [36] Bickford WB, Strom BT. Vibration of plane curved beams. J Sound Vib 1975;39(2):135–46.
- [37] Kawakami M, Sakiyama T, Matsuda H, Morita C. In-plane and out-of-plane free vibrations of curved beams with variable sections. J Sound Vib 1995;187(3):381–401.
- [38] Xuechang H, Hongxing H, Yu W, Zhipeng D. Research on wave mode conversion of curved beam structures by the wave approach. J Vib Acoust 2013;135(3).
- [39] Le Bot A, Ichchou MN, Jezequel L. Energy flow analysis for curved beams. J Acoust Soc Am 1997;102(2):943–54.
- [40] Lee S, Mace BR, Brennan MJ. Wave propagation, reflection and transmission in curved beams. J Sound Vib 2007;306(3):636–56.
- [41] Jeong C, Ih J. Effects of nearfield waves and phase information on the vibration analysis of curved beams. J Mech Sci Technol 2009;23(8):2193–205.
- [42] Fong J, Lowe MJS. Curvature effect on the properties of guided waves. AIP Conf Proc 2004;700:126–33.
- [43] Rose JL. Ultrasonic guided waves in solid media. Cambridge University Press; 2014.
- [44] Zhou WJ, Ichchou MN. Wave propagation in mechanical waveguide with curved members using wave finite element solution. Comput Methods Appl Mech Eng 2010;199(33–36):2099–109.
- [45] Demma A, Cawley P, Lowe MJS. Guided waves in curved pipes. AIP Conf Proc 2002;615(1):157–64.
- [46] Aristegui C, Cawley P, Lowe M. Reflection and mode conversion of guided waves at bends in pipes. AIP Conf Proc 2000;209(1):209–16.
- [47] Sanderson RM, Hutchins DA, Billson DR, Mudge PJ. The investigation of guided wave propagation around a pipe bend using an analytical modeling approach. J Acoust Soc Am 2013;133(3):1404–14.
- [48] Zak A, Krawczuk M. Certain numerical issues of wave propagation modelling in rods by the Spectral Finite Element Method. Finite Elem Anal Des 2011;47(9):1036–46.
- [49] Patera AT. A spectral element method for fluid dynamics: Laminar flow in a channel expansion. J Comput Phys 1984;54(3):468–88.
- [50] Canuto C, Hussaini MY, Quarteroni A, Zang TA. Spectral methods in fluid dynamics. Springer; 1988.
- [51] Kudela P, Zak A, Krawczuk M, Ostachowicz W. Modelling of wave propagation in composite plates using the time domain spectral element method. J Sound Vib 2007;302(4):728–45.
- [52] Komatitsch D, Vilotte JP. The spectral element method: an efficient tool to simulate the seismic response of 2D and 3D geological structures. Bull Seismol Soc Am 1998;88(2):368–92.
- [53] Dauksher W. The use of spectral methods in predicting the reflection and transmission of ultrasonic signals through flaws. Rev Prog Quant Nondestruct Eval 1996;15(3):33–40.
- [54] Zak A, Krawczuk M, Ostachowicz W. Propagation of in-plane waves in an isotropic panel with a crack. Finite Elem Anal Des 2006;42(11):929–41.
- [55] Sridhar R, Chakraborty A, Gopalakrishnan S. Wave propagation analysis in anisotropic and inhomogeneous uncracked and cracked structures using pseudospectral finite element method. Int J Solids Struct 2006;43(16):4997–5031.
- [56] Kumar Munian R, Roy Mahapatra D, Gopalakrishnan S. Lamb wave interaction with composite delamination. Compos Struct 2018;206:484–98.
- [57] Ostachowicz W, Kudela P, Krawczuk M, Zak A. Guided waves in structures for SHM: the time-domain spectral element method. John Wiley & Sons; 2011.
- [58] Su Z, Ye L. Identification of damage using lamb waves: from fundamentals to application, vol. 48. Berlin: Springer; 2009.